These corollaries are useful for avoiding dangerous language when discussing MEG/EEG inversions. Being aware of these corollaries will hopefully enable more robust and accurate statistics and inferences.

2.6.1 Comparison of MEG and EEG

The basic findings when comparing MEG, EEG and their combination replicated those of (Liu, Belliveau, and Dale, 1998; Liu, Dale, and Belliveau, 2002), particularly in that the combination of both MEG and EEG generally improves inverse solutions, with some regions benefiting more than others, as apparent in Figure 2.8. The CLE was most affected by the extremity of the source location, i.e. the more superficial sources had larger errors than deeper sources, as did sources that were at the anterior and posterior extrema. The AAD was most affected by the orientation of the source location, with larger errors at both the crests of gyri and the troughs of sulci. The SAE recovered the most signal for the most superficial sources, without reflecting the same extrema bias the CLE did. The TAE was greatest in the troughs of the sulci, reflecting susceptibility to both the orientation and the depth of sources. Nonetheless, while combining EEG and MEG sensors improved the CLE, AAD, and TAE metrics, they did not improve the overall SAE. For MEG, the number of sensors (306) already sufficiently samples the distribution approaching the limit of the applied amplitude. All that adding more sensors does is change the distribution of that amplitude (improving performance on the other metrics). Meanwhile, for EEG only, there is still a lot of room for improvement in the SAE, due to the very low number of sensors ($8 - 456$). In terms of a researcher's decision about how many EEG electrodes to combine with an existing MEG system, the rate of improvement in all four metrics diminished significantly beyond 118 electrodes.

The results from the ROI analysis of FFA and OFA revealed some interesting effects. The improvement in CLE, AAD, and TAE from adding EEG to MEG was greater for the deeper FFA than the more superficial OFA. This is important, because the ability to localise deep sources is a common concern of EEG and MEG. The SAE was the only metric for which the more superficial OFA source showed greater improvement with increasing numbers of EEG sensors than the

more deeper FFA source. Interestingly, there was little change in the TAE for the OFA as the number EEG sensors added to MEG increased, suggesting that improvements in the other metrics can occur without affecting the total area "active".

2.6.2 Future work

Future areas to explore, in terms of assessing the modern forward model, include:

- the effects of noise, particularly noise-normalised inverse solutions
- the effects of errors in head position estimation
- the effects of errors in the forward solution calculations (e.g. BEM and FEM models, particularly for EEG and EMEG)
- the effects of more typical (less idealized) EEG coverage (and the question of optimal electrode location for specific ROIs, given only a limited number, or constraints on preparation time)

Another potential area for future work is to see if there is any way the multimodal nature of modern Forward Model's PSFs can be utilized to benefit MEEG research (see chapter 5).

Chapter 3

Face Processing Study

3.1 Forward

The purpose of this chapter is to describe the multimodal dataset (containing MEG, EEG, MRI and fMRI modalities) that is used throughout the remaining chapters of this thesis. These data have also been made freely available for other researchers, via a website, as part of their award in the BIOMAG 2010 Connectivity Challenge.

3.2 Introduction

One of the strongest contributions MEG can make to neuroscience is showing, non-invasively, how brain regions act, and interact, at the millisecond timescale. The domain of face processing is a good domain to study these, because the key anatomical regions within the ventral visual stream (and beyond) are well-established. The "core" network (Haxby, Hoffman, and Gobbini, 2000) is composed of three distinct regions in posterior occipitotemporal cortex: the Occipital Face Area (OFA), Fusiform Face Area (FFA) and Superior Temporal Sulcus (STS). This network has been examined extensively with fMRI, extracranial EEG, intracranial EEG, TMS and MEG, in both healthy individuals and prosopagnosics (Halgren et al., 2000; Puce et al., 1997; Puce, Allison, and McCarthy, 1999; Henson et al., 2003; Rossion et al., 2003) , as well as single-cell

recording/lesion/fMRI studies in the nonhuman primate (O Scalaidhe, Wilson, and Goldman-Rakic, 1999; Tsao, Moeller, and Freiwald, 2008). However, no study to date has combined fMRI, EEG and MEG on the same set of healthy participants performing the same experimental paradigm. The strong prior expectations about the Regions Of Interest (ROIs) involved in face processing, coupled with multiple imaging methods on the same brains, should allow better examination of differences in source localization across the different techniques.

Based on the psychological model of Bruce and Young (Bruce and Young, 1986), Haxby, Hoffman, and Gobbini, 2000 proposed that the "core" system includes three processing routes: a ventral route from the OFA to the FFA, a lateral route from OFA to STS, and third route from the FFA to the STS. Figure 3.1 shows the original representation of the Haxby, Hoffman, and Gobbini network. They hypothesized that the ventral route is involved in processing the invariant aspects of faces, as necessary for recognizing an individual from different viewpoints, expressions, etc. It is damage to this route that tends to produce associative prosopagnosia (Rossion, 2008), or, in the case of the OFA, face identification problems in healthy individuals when targeted by TMS (Pitcher et al., 2007). Haxby, Hoffman, and Gobbini hypothesized that the lateral route, on the other hand, is associated with processing the more changeable aspects of faces, for example discriminating different facial expressions on the same face. These ROIs appear to be strongest/most reliable in the right hemisphere, which is consistent with prosopagnosia being more likely following right hemisphere lesions (Landis et al., 1986) , and with behavioral evidence for a left visual field advantage in face processing in healthy individuals (Young et al., 1985; Hillger and Koenig, 1991). Nonetheless, neuroimaging often reveals concurrent activation in the left hemisphere too.

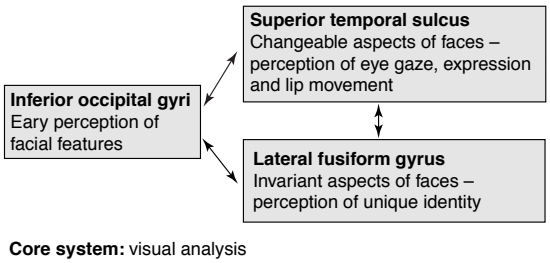

Figure 3.1: This is a replication of the "Core Visual Network" portion of Figure 5 from Haxby, Hoffman, and Gobbini's 2000 paper, which shows the core of their model of the human neural system for face perception.

There are also several other brain regions often activated in neuroimaging studies of face processing (such as more anterior ventral temporal regions, amygdala, ventral prefrontal cortex; e.g. Ishai 2008), but these are generally associated with secondary aspects of face processing (such as detection of emotional status), which, though often triggered automatically by faces, may not be specific to faces (i.e. occur for other stimuli too). Haxby brackets these in the "extended" face system, but these regions are not considered further here (particularly given that they are not apparent in the specific comparisons of fMRI and MEG/EEG data considered here, as shown later).

While fMRI has identified the key regions in humans, there is an older and extensive EEG (and to a lesser extent MEG) literature that has focused on the temporal dynamics associated with different stages of face processing. The earliest evoked response that reliably distinguishes faces from visually-matched non-face stimuli starts around $150ms$, and is maximal around $170ms$ (the "N170" in EEG or "M170" in MEG). The N/M170 does not typically differ according to whether the face has been seen before, or whether it is recognized as familiar (Bentin et al., 2007; Henson et al., 2003; Schweinberger et al., 2002), suggesting that it reflects a relatively early stage of categorization of faces vs non-faces. Again, there are other ERP/ERF components related to face-processing (e.g. related to person identification and expression recognition), particularly at longer latencies, but these are less relevant to the present analyses (that focus on the first few hundred milliseconds post-stimulus). There are also induced effects, demonstrated using time-frequency analyses (e.g. in gamma range (Zion-Golumbic et al., 2008)), though these effects are typically lower in SNR, with the majority of energy in lower frequencies coming from the evoked component, i.e. N/M170 (Henson et al., 2005). Evoked responses are therefore the focus of this work.

The N/M170 is generally maximal around posterior, occipitotemporal sites (when using a nose reference with EEG, or planar gradiometers with MEG), and is often stronger on the right. It has been associated with activity in inferior occipito-temporal regions (Bentin et al., 2007; Schweinberger et al., 2002), though the source localization methods used in these studies were limited (e.g. equivalent current dipoles and spherical forward models). More recent efforts using combined EEG and MEG (Henson, Mouchlianitis, and Friston, 2009) have revealed two

likely sources in ventral and lateral occipito-temporal cortex, but have not yet managed to separate all three OFA, FFA and STS ROIs (most likely because of high cross-talk; see chapter 5). Indeed, intracranial ERP studies have suggested that the N200 (an effect believed to correspond to the extracranial N170, being delayed only because the patients in these studies were medicated) occurs in all three of these regions (Puce, Allison, and McCarthy, 1999).

The definition of the N/M170 can be based on a range of different comparisons, such as faces vs non-face objects (e.g, houses), though these are not always matched for low-level visual properties. Here we used meaningless, non-objects as control stimuli, which were created by phase-scrambled Fourier-transformed versions of the faces, in order to match the 2D spatial frequency power spectrum. In fact, the paradigm, which was based on Henson et al., 2003, included several other trial-types (e.g. famous vs non-famous faces, initial vs repeated presentations, as detailed in Methods section below). However, for the remaining chapters, these conditions were collapsed, given prior evidence that face familiarity and repetition do not affect the N/M170 (Henson et al., 2003) (and given that the focus of the following chapters was on methods for extracting reliable source data for these two conditions, rather than on neuroscientific claims about various aspects of face processing). This maximized the number of trial-types (giving several hundred face trials and several hundred scrambled face trials), hence maximizing the SNR for the basic N/M170 effect.

3.3 Methods

3.3.1 Materials

The stimuli were greyscale photographs of faces of 149 famous people (due to an error one famous person had two sets of images presented) and 150 nonfamous people (unknown to participants), compiled from several sources (see (Eger et al., 2005) for more details). Half of the faces were male, half female. The famous faces were selected in order to be recognized by the majority of British adults. Nonfamous faces were approximately matched to famous faces in terms of their sex and age (by visual judgement). All photos were matched and cropped to show

only the face. The photos covered a wide range of hairstyles (though long hair was cropped), expressions (though mainly happy or neutral), and orientations (though all were taken from between a full-frontal to 3/4-view perspective).

There were two photographs of each face, taken from slightly different viewpoints, lighting conditions, etc. One set of photographs was used for the M/EEG recording session, and the other was used for the fMRI recording session. While use of faces of the same people across the two sessions (which were separated by approximately 3 months) is likely to induce neural effects of that repetition, such effects are unlikely to affect the early N/M170 response of interest (Henson et al., 2003).

A random half of these stimuli (75 famous and 75 nonfamous) were used to generate 150 scrambled faces. These were scrambled by taking the 2D-Fourier transform of the faces, permuting the phase information, and then inverse-transforming back into the image space. To match the overall approximate shape and size of the original faces, the scrambled images were finally cropped to a mask created by a combination of one famous and one nonfamous face (see Figure 3.2 for an example). Although this masking meant that the power density spectrum of the scrambled faces no longer exactly matched that of the original faces, matching the visual angle of the two types of stimuli was deemed more important, e.g, to minimize differences in eye-movements.

3.3.2 Basic Design

The basic design of the experiment is based on Henson et al., 2003. A typical sequence and timing of trials is shown in Figure 3.2. Stimuli were projected onto a screen approximately 1.3m in front of the participant, subtending horizontal and vertical visual angles of approximately 3.66° and 5.38° respectively. The photographs were presented against a black background, with a white fixation cross in the center. The start of a trial was indicated by the appearance of a fixation cross for a random duration between 400ms and 600ms, after which the critical stimulus (face or scrambled face) was superimposed for a random duration between $800ms$ and $1000ms$. The random jitter before stimulus onset was to reduce aliasing of ongoing neural oscillations (at least above approximately $5Hz$)

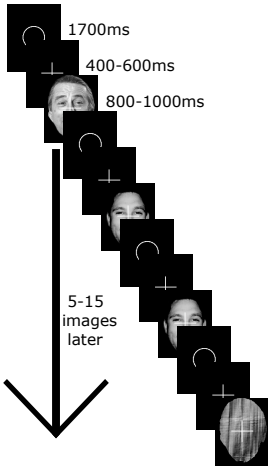

Figure 3.2: The experimental design.

and to avoid any pre-stimulus phase resetting (Barry et al., 2003). The offset jitter was to average out visual offset effects (again, at least above $5Hz$) and to avoid pre-stimulus (in this case the white circle acts as a stimulus) phase resetting. The interstimulus interval comprised a central white circle for $1700ms$. Participants were told to fixate centrally throughout the experiment, with the change from central circle to central cross helping to prepare the participant for each stimulus. They were also instructed to try to not blink during the cross-hair or stimulus (but to blink freely during the circle).

Each image was presented twice, with the second presentation occurring either immediately after (Immediate Repeats), or after 5–15 intervening stimuli (Delayed Repeats), with 50% of each type of repeat. The reason for manipulating this repetition lag was because it has been shown to modulate repetition-related effects (Henson et al., 2004), though this manipulation is not studied further in this thesis.

To ensure attention to each stimulus, participants were asked to press one of two keys with either their left or right index finger (assignment counter-balanced across participants). Their key-press was based on how symmetric they regarded each image: pressing one or the other key depending whether they thought the image was "more" or "less" symmetric than average. The range of symmetries (hence idea of average symmetry) was made apparent from a practice session

of at least 23 separate photos (not used in the main experiment). Participants continued this practice until they were comfortable with the task. The reason for using this task was because it can be performed equally well on face and non-face stimuli (Henson et al., 2003). Because this symmetry judgment is somewhat subjective however, there were no behavioral data of interest (other than mean reaction times, which were typically $955ms$ with a standard deviation $283ms$). Only trials with button presses more than $300ms$ after stimulus onset were included in the neuroimaging analysis (to exclude motor activity from spurious key presses).

3.3.3 Participants

24 people participated in at least one component of the experiment (plus one pilot participant); however, due to 3 participants dropping out of the study, and poor MEG/EEG data in 2 participants (one due to magnetic artifacts and the other due to a software error resulting in data loss), only 19 participants' data were analyzed. 8 of the participants were female, and 11 were male, with an age range of 20–35 years. All were Caucasian except for one Asian participant.

The study was approved by Cambridge University Psychological Ethics Committee (reference CPREC 2005.08). Written informed consent was obtained from each participant prior to and following each phase of the experiment. Participants also gave separate written consent for their anonymized data (once structural MRIs were de-faced) to be freely available on the internet.

The first 16 people participated in the MEEG phase first and the MRI phase second, while the last three participated in the MRI phase first and the MEEG phase second (thus order of modality was not fully counterbalanced). All had a gap of at least three months between their first and second visits, to help limit participants remembering faces from the previous visit.

3.3.4 MEEG data

3.3.4.1 Acquisition Parameters

Following the practice, stimuli in the MEEG visit were presented in six 7.5 minute sessions. Both the MEG and EEG were measured in a light magnetically shielded room utilizing an Elekta Neuromag Vectorview 306 system (Helsinki, FI). Four head-position indicator coils were attached to the EEG cap and stimulated with sinusoidal currents (293-321 Hz). A 70 channel Easycap EEG cap was used to record the EEG data simultaneously, with electrode layout conforming to the extended 10-10% system. A 3D digitizer (Fastrak Polhemus Inc., Colchester, VA, USA) was used to record the locations of the EEG electrodes, the HPI coils and approximately 50-–100 "head points" along the scalp, relative to three anatomical fiducials (the nasion and left and right pre-auricular points).

Both data sets were acquired at an 1100 Hz sampling rate with a lowpass filter at 350Hz and no highpass filter. The EEG data were referenced to the nose and an amplifier ground electrode was placed at the left collar bone. Two sets of bipolar electrodes were used to measure electro-oculogram (EOG) and another set was used to measure the electro-cardiogram (ECG). Twenty seconds of raw data were collected at the start of each run in order to facilitate automatic bad channel detection via the Neuromag Maxfilter software.

After the MEEG Acquisition, a simple self-paced behavioral task was run, in which participants saw each of the 300 faces again, but now used three buttons to indicate whether 1) they had not seen the face before the experiment, 2) the face looked familiar, but they could not remember from where, or 3) they knew the face, i.e. could remember definite fact about them, such their job, a movie they were in, their name, etc. The results of this test were used to remove trials in the main experiment for which a participant thought that a Nonfamous face was familiar (rated 2 or 3), or that a Famous face was unfamiliar (rated 1). Though not directly relevant to the present focus on intact versus scrambled faces, this procedure should optimise future comparisons of familiar vs unfamiliar faces. Thus in fact, there were 9 trial-types coded in the data (3 types of face: Familiar, Unfamiliar and Scrambled, crossed with 3 types of occurrence: Initial, Immediate Repeat and Delayed Repeat), though only the Intact (Familiar and Unfamiliar)

vs Scrambled face trials are analyzed here (averaged across occurrence).

3.3.4.2 Data Pre-Processing

Bad channels were marked by visual analysis (of the entire raw data). This revealed a mean of 2 bad channels per session, with a minimum of 0 and a maximum of 12 (across all participants, sessions and sensor types). External noise was removed from the MEG data using the temporal extension of Signal-Space Separation (SSS) (Taulu and Simola, 2006) as implemented with the MaxFilter software (Version 2.0 Elekta-Neuromag) with $4s$ windows and .98 correlation. Maxfilter was also used to reconstruct any bad MEG sensors, and to realign the MEG data to the head position at the start of each session, compensating for movement every $200ms$ within each session. The mean translation between the first session and all other sessions ranged from $0.59mm$ to $7.95mm$ across participants (median = $3.53mm$). The head position for the first session was utilized as the position for all subsequent forward modeling.

The data were then preprocessed in MNE Version 2.6.0 (http://martinos.org/mne/), starting with band-pass filtering from $0.1-45Hz$, before being epoched from $-200ms$ to $900ms$, with the mean across the first $200ms$ being subtracted. The EEG data were re-referenced to the average of all non-bad electrodes. Epochs in which the amplitude range exceeded $150_{\mu V}$ for EOG, $125_{\mu V}$ for EEG, 5_{pT} for Magnetometers, or $200_{pT/m}$ for Gradiometers were rejected. The remaining epochs of each of the 9 trial-types were then averaged according to whether Intact (Face) or Scrambled, weighted by the number of trials of each type (thereby producing results the same as if the original trials were categorized solely by whether intact or scrambled). The final averages effectively came from 398 face trials and 246 scrambled face trials on average across participants.

3.3.5 MRI data

3.3.5.1 Acquisition Parameters

All the MRI data were collected from a Siemens 3T TIM TRIO (Siemens, Erlangen, Germany). A standard 1mm isotropic T1-weighted MPRAGE was acquired on each of the participants (TR $2250ms$, TE $2.98ms$, TI $900ms$, and flip

angle 9°). Two bandwidth-matched Multi-Echo FLASH sequences (also $1mm$ isotropic) were acquired at both 5° and 30° (TR $20ms$, TE $1.85ms$; $4.15ms$; $6.45ms$; $8.75ms$; $11.05ms$; $13.35ms$; $15.65ms$). All of the EPI data collected utilized 33, 64×64, $3mm$-thick axial slices resulting in voxel sizes of 3x3x3mm (TR $2000ms$, TE $30ms$, flip angle 78°) with a 25% distance spacing between slices (increased where necessary to accommodate head size), resulting in inter-slice spacing between $0.75mm$ and $1.05mm$.

The first 5 volumes were discarded in order to avoid transient T1 effects, with the stimuli starting with the start of the sixth volume. The trial-timing was slightly different from the MEG experiment, in that the data were acquired across 9 (rather than 6) sessions (each lasting 7mins) and during each session, 5 blocks of 20s of fixation were equally distributed (resulting in stimulation blocks of $50s$ with $25s$ stimulation blocks starting and ending each run). This provided an opportunity to estimate the BOLD evoked responses versus a fixation baseline.

A fieldmap was also collected for each participant, though not used as the distortion in the EPI data was minimal. Diffusion Weighted Images were also acquired on 13 of the subjects (64 directions with $2mm$ isotropic voxels) during a separate visit, but are not analyzed in this thesis.

3.3.5.2 Structural MRI Analysis

The MPRAGEs were segmented the brain into grey and white matter surfaces utilizing FreeSurfer (`http://surfer.nmr.mgh.harvard.edu/`) (Dale, Fischl, and Sereno, 1999; Fischl, Sereno, and Dale, 1999; Fischl, Liu, and Dale, 2001). A three-layer, boundary element model (BEM) model was built, using the multi-echo FLASH data to create the inner skull and outer skull layers, and the MPRAGE data to create the outer skin layer (see chapter 4 for a more detailed description of this process). The forward model calculations were made using MNE version 2.6 (`http://martinos.org/mne/`). The forward model was calculated utilizing fixed dipole orientations normal to the cortical surface (sampled every $1mm$). Each of the BEM surfaces was downsampled to a 4th order icosahedron in order to enable the computations.

The MPRAGE data were also analyzed in SPM8 (`http://www.fil.ion.ucl.`

ac.uk/spm), using a unified segmentation and normalization process, which provided a spatial transformation (warps) between each individual's brain and a template brain in Talairach space produced by the Montreal Neurological Institute (MNI) (Ashburner and Friston, 2005). The number of tissue segments used in this process was increased (from the default grey matter, white matter, CSF and other) to include bone and skin, thereby extending the warps to include matching of the skull/scalp, such that canonical surfaces for BEMs could also be created within SPM (see chapter 4).

3.3.5.3 functional MRI Analysis

The EPI data for each participant were first coregistered (spatially realigned) to the first volume to adjust for movement. The mean across all volumes was then coregistered with that participant's MPRAGE image, and the rigid-body transformation applied to all volumes, which were then resampled to the same space as the first volume. The different slice acquisition times were corrected by temporally realigning to the middle slice, then all volumes transformed into MNI space using the warps created during the above normalization of the MPRAGE image, and resampled to $3mm$ isotropic voxels. Finally, the volumes were smoothed with an $8mm$ Full Width at Half Maximum (FWHM) Gaussian kernel (final smoothness approximately 13.9x13.8x13.1mm).

Statistical analysis was performed in a two-stage approximation to a Mixed Effects model. In the first stage of modeling the BOLD timeseries within each participant, neural activity was modeled by a delta function at each stimulus onset. The resulting BOLD response was modeled by convolution of these delta functions by a canonical Hemodynamic Response Function (HRF). The resulting time-courses were down-sampled at the midpoint of each scan to form regressors in a General Linear Model (GLM). For each of the 9 runs, 44 regressors were used to model all combinations of condition (including invalid trials where no keypress was recorded), together with the 6 rigid-body movement parameters from the above spatial realignment step (in order to capture residual (linear) movement artifacts). Voxel-wise parameter estimates for these regressors were obtained by Restricted Maximum-Likelihood (ReML) estimation, using a temporal high-

pass filter (cut-off $128s$) to remove low-frequency drifts, and modeling temporal autocorrelation across scans with an AR(1) process. Images of contrasts of these parameter estimates were created that averaged across the different types of Intact and Scrambled faces, and across the 9 sessions, weighted by the number of events within each regressor (as in the MEEG analysis).

In the second stage of modeling across participants, these contrast images for Intact and Scrambled faces for each participant were entered into a GLM corresponding to a paired T-test. Statistical Parametric Maps (SPMs) were created of the T-statistic at each voxel for the two contrasts of Intact > Scrambled and Scrambled > Intact. The SPMs were thresholded for voxels whose statistic exceeded a peak threshold corresponding to $p < .05$ corrected for family-wise error (FWE) across the whole brain using Random Field Theory (RFT). Stereotactic coordinates of the maxima within the thresholded SPMs correspond to the MNI template.

3.4 Results

3.4.1 MEEG

3.4.1.1 Grand Averages

We begin by examining the grand averages across participants for each sensor for the Intact and Scrambled conditions. These are shown for the Magnetometers in Figure 3.3, the Gradiometers in Figure 3.4 and the EEG electrodes in Figure 3.5, using a flattened map with anterior sensors located at the top, and right hemisphere sensors located on the right. The evoked responses for the two conditions begin to diverge around $150ms$, coinciding with the start of the second peak component, the M/N170, after which they remain apart for the length of epoch. This divergence is most noticeable over right and left temporal Magnetometers, the right occipito-temporal gradiometers, and left and right occipito-temporal electrodes. The waveforms for sensors selected close to these maxima are expanded in Figure 3.6, to illustrate the temporal profile more clearly.

The topography for the difference between Intact and Scrambled faces averaged across a timewindow of $150-190ms$ (centered on the M/N170 peak) is shown

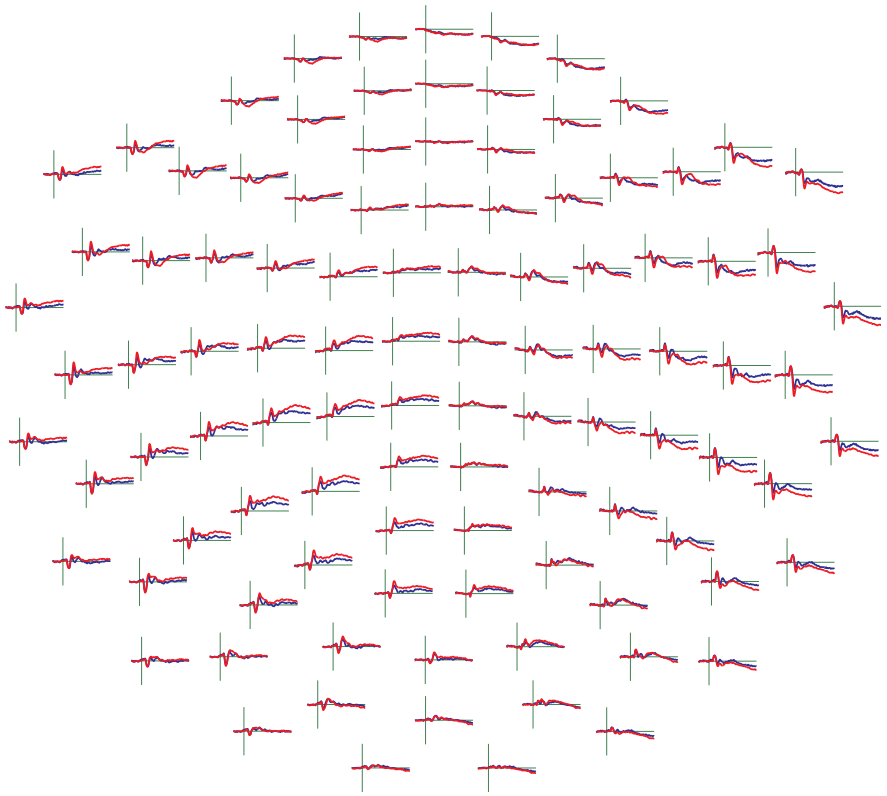

Figure 3.3: The grand average across participants of the magnetometer data for Intact (red) and Scrambled (blue). The data go from $-200ms$ to $900ms$ (with a vertical green line indicating stimulus onset at each sensor). The bottom and top of the vertical bar correspond to -300 and $+300fT$, respectively.

for each sensor-type in Figure 3.7. Here one can see the different properties of the sensors, with the magnetometers showing two polar patterns, each containing a region of in-going and out-going magnetic flux. The RMS of the gradiometers shows two peaks that are maximal in the left and right posterior sensors (with the right sensors showing a larger peak). The EEG shows two dipolar patterns of activity with the negative components over the left and right posterior sensors, and a common positive pole around the central sensors. The gradiometer and EEG sensor patterns highlight a likely explanation of the Magnetometer pattern, namely one source in the posterior part of each hemisphere (likely located under the peaks of the planar gradiometer activity). Furthermore, if one rotates the EEG dipolar pattern ninety degrees, two of the EEG peaks would line up with

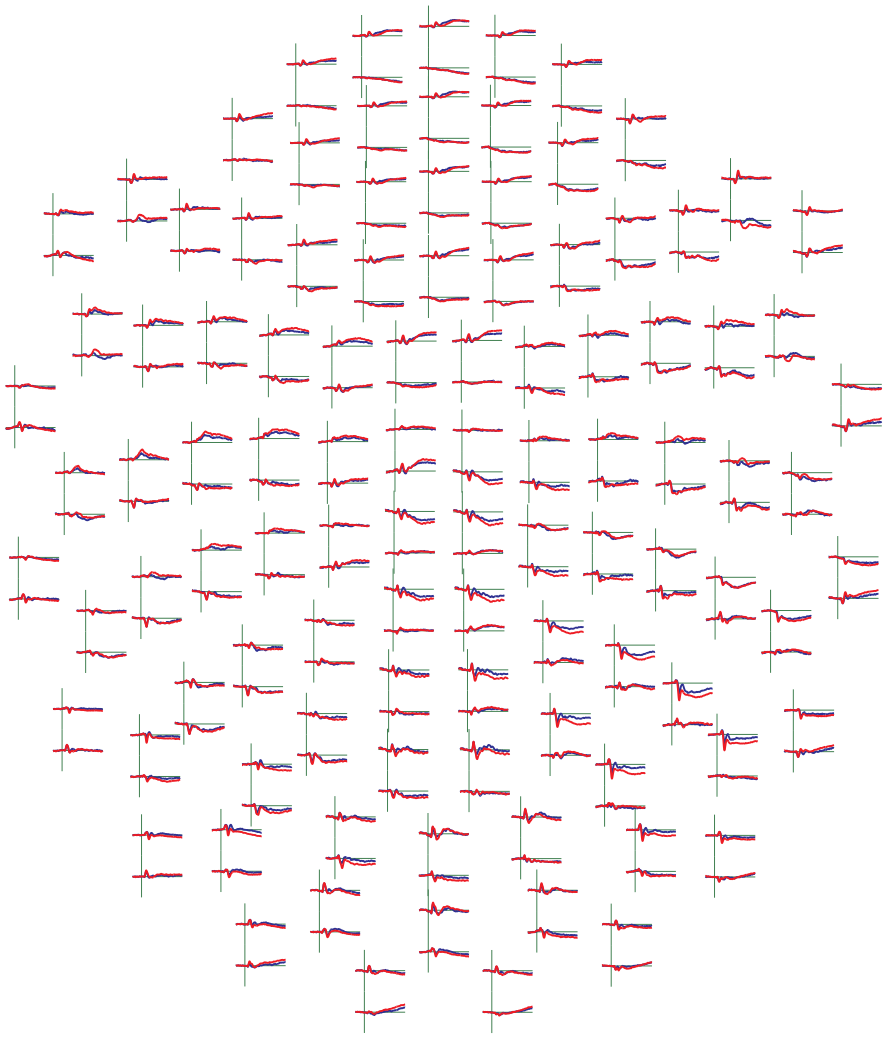

Figure 3.4: The grand average across participants of the gradiometer data for Intact (red) and Scrambled (blue). The two gradiometers from each pair are shown one above the other (with the lower number sensor above the higher). The data go from $-200ms$ to $900ms$ (with a vertical green line indicating stimulus onset at each sensor). The bottom and top of the vertical bar correspond to -66.7 and $+66.7fT/cm$, respectively.

the magnetometer peaks, while the other ends of the dipolar patterns would end up outside the sensor arrays. This suggests that the magnetometer pattern reflects half of two dipolar patterns of activity (corresponding to the left and right occipitotemporal responses to the stimuli).

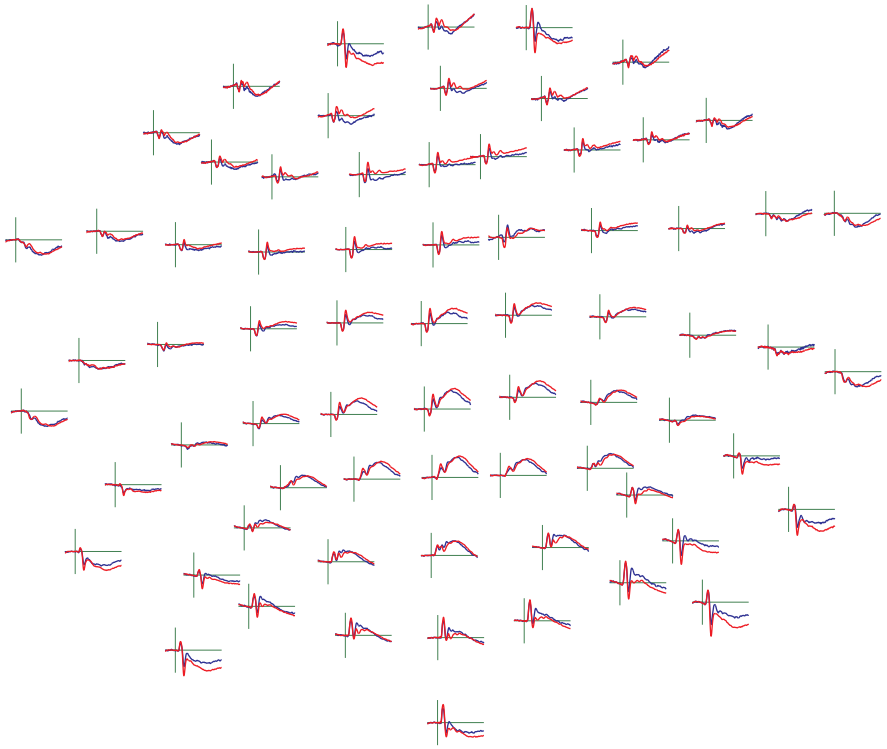

Figure 3.5: The grand average across participants of the EEG data for Intact (red) and Scrambled (blue). The data go from $-200ms$ to $900ms$ (with a vertical green line indicating stimulus onset at each sensor). The bottom and top of the vertical bar correspond to -7.5 and +7.5 μV, respectively.

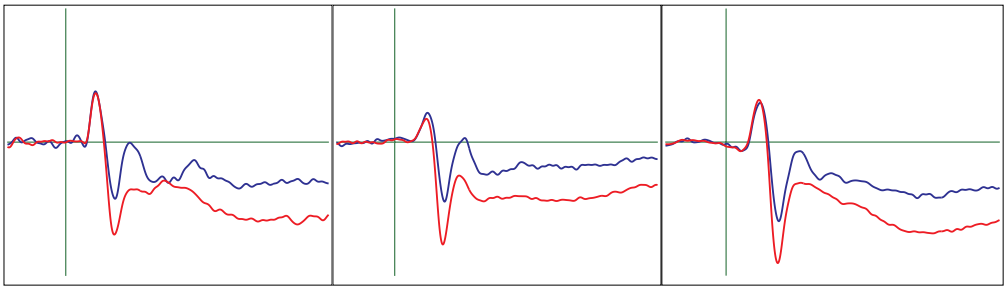

(a) Magnetometer 2421 -100_{fT} to 100_{fT} (b) Gradiometer 2523 $-67_{fT/cm}$ to $67_{fT/cm}$ (c) EEG Sensor 65 $-12.5_{\mu V}$ to $12.5_{\mu V}$

Figure 3.6: The plots of single sensors near the maxima of the M/N170. The time ranges from $-200ms$ to $900ms$.

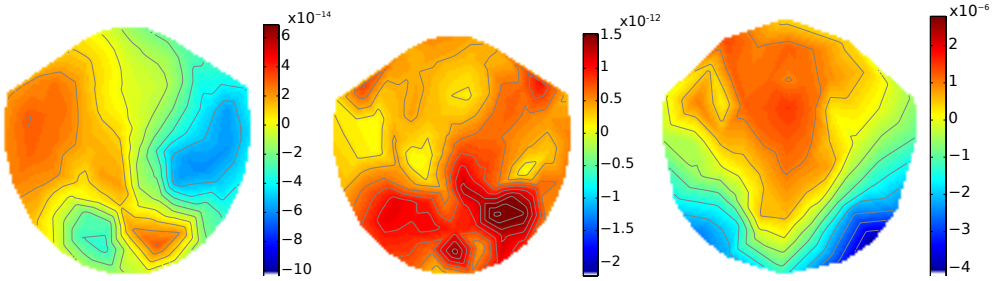

(a) Magnetometer T (b) Gradiometer RMS T/m (c) EEG Sensors V

Figure 3.7: Topographic plots of sensors at 166ms. For the gradiometer data (middle panel), the root-mean-square (RMS) of the values of the two planar gradiometer pairs was taken at each location.

3.4.1.2 Sensor SPMs

To establish the reliability of these effects across participants, a space-time analysis was performed in SPM8. This entails projecting each sensor type to a 2D plane, interpolating the data to a 32×32 grid, and then tiling these grids to form a third dimension of peristimulus time. For the gradiometer data, the root-mean-square (RMS) of the data was taken across the two gradiometers at each location (to give a single, scalar measure of in-plane gradient at that location). Such 3D images for each participant and condition were then entered into a GLM for a paired T-test, in which both tails were tested (given that polarity was not of main interest) using an F-contrast. The resulting SPMs of the F-statistic were corrected for multiple comparisons across space and time using RFT. The results are shown in Figure 3.8 (note that the sections on the left showing the 2D topography for a selected timepoint are rotated by 90 degrees with respect to the above figures, such that the nose would be to the right).

What is clear from each SPM is that the maximally reliable difference between Intact and Scrambled (i.e. most consistent in size, timing and location across participants) occurs around 170ms, and over those sensors that also show the maximal effect size (as in Figure 3.7). There are reliable differences later too (corresponding to the sustained divergence noted above), but these are not as reliable, particularly in the gradiometer RMS. Because of the high SNR and focal spatio-temporal localization of the M/170 effect, we concentrate on this effect for

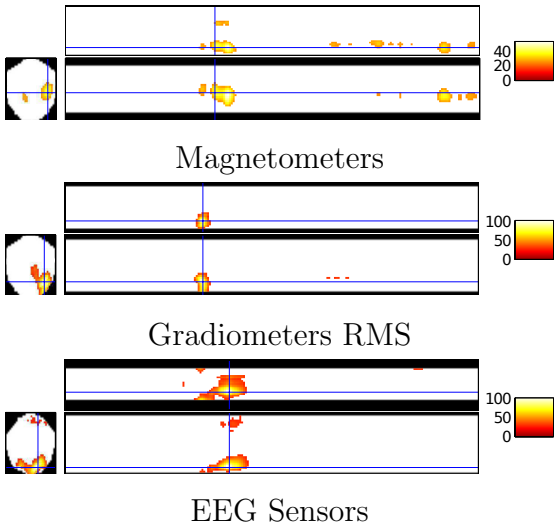

Figure 3.8: Sections through the 3D SPMs for the F-tests of Intact vs Scrambled across participants for each sensor type. The SPMs have been thresholded at $p < 0.05$ FWE-corrected for the peak of the statistical map, with the legend showing (suprathreshold) F-values (with df's of (1,18)). The sections are centered on the cross-hair, corresponding to the maximal statistic within each SPM (at $195ms$, $165ms$ and $235ms$ for magnetometers, gradiometers and EEG respectively). The two sections on the right within each panel show time $\times$ space (posterior–anterior slice on the top; left–right slice on the bottom); the section on the left within each panel shows the 2D topography for the peak timepoint. Time goes left to right from $-200ms$ to $900ms$.

the remainder of the thesis.

3.4.1.3 Inversion Results

For the canonical source reconstruction in SPM8, a head-model was first created for each subject by warping scalp, outer skull, inner skull and cortical surfaces of a template brain in MNI space, based on the spatial normalization of each subject's T1 MRI image (as for the fMRI analysis above). The MEG and EEG data were then coregistered with the T1 MRI image using an iterative closest point algorithm for 1) the fiducial positions marked on the T1 and digitized during the MEEG experiment and 2) the scalp surface and the additional head-points also digitized (excluding points on the nose and face, which are not included in SPM's surfaces). The resulting coregistered "canonical" meshes and sensor positions were then used to create a forward model using a single shell approximation for the MEG data (Nolte, 2003) and a three-shell Boundary Element

Model (BEM) for the EEG data (Berg and Scherg, 1994). The cortical sources of evoked responses to faces and scrambled faces from $-100ms$ to $+300ms$ (using a Hannning window) were estimated using a common minimum-norm prior on the sources, and separate white-noise components for the sensor noise of each sensor-type (Henson, Mouchlianitis, and Friston, 2009). The total evoked energy for each condition between $150 - 190ms$ (i.e. around N170) was then calculated for each vertex, interpolated to voxels within a 3D volume in MNI space, and smoothed by a $8mm$ FWHM Gaussian. These smoothed, normalized images were then entered into the same GLM for a paired T-test that was used for the sensor statistics and fMRI statistics above.

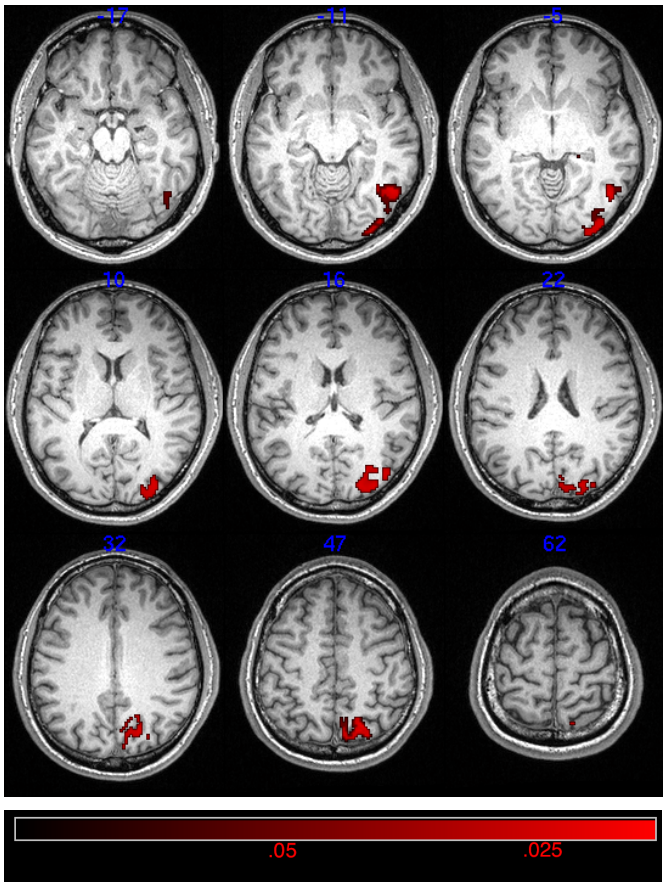

Figure 3.9: The results of an uncorrected T-test (Intact > Scrambled) with a 10 connected voxel threshold. The scale bar shows the p-values of the comparison in MNI space of all 18 participants. The slices shown were selected based on the fMRI results and are identical to those in Figure 3.11.

Figure 3.9 shows the group results for a standard SPM 8 Canonical L2 minimum norm inversion, with 20,484 vertices for each participant. These results highlight several problems with this type of analysis of inverted data. There are

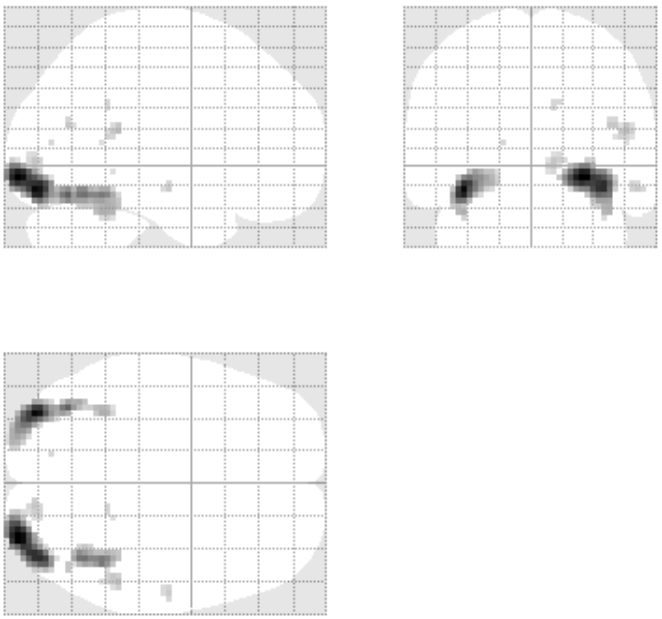

Figure 3.10: Maximal Intensity Projections (MIPs) of three orthogonal sections in MNI space showing clusters of at least 10 voxels that survive $p < .05$ FWE-corrected for peak of the SPM for the contrast Intact > Scrambled. No voxels survived correction for the opposite contrast. Labels indicate which ROI is represented by each cluster.

a few active regions in the right hemisphere, but none in the left hemisphere, and the correspondence with the fMRI group results from the same participants is poor (see next section).

3.4.2 Univariate fMRI Results

The corresponding SPM for the fMRI data is shown in Figure 3.10 and in Figure 3.11. Greater event-related BOLD responses were found in bilateral ventral occipitotemporal clusters corresponding to OFA (more posterior) and FFA (more anterior) (these clusters were separate on the right, but merged on the left). The only other activation was in the right STS. There was no evidence (at the same corrected threshold) for greater BOLD responses to Scrambled than Intact.

3.5 Discussion

These data show robust effects (in fMRI and in MEEG sensor space), which replicate previous findings e.g. (Henson et al., 2003). They represent a good

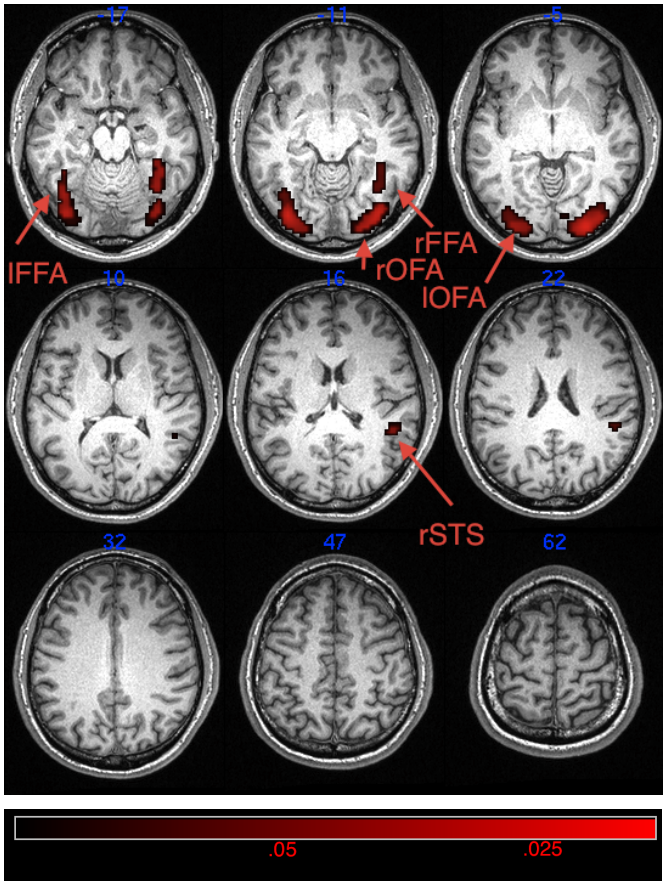

Figure 3.11: The T-Test results in MNI space showing clusters of at least 10 voxels that survive $p < .05$ FWE-corrected for the peak of the SPM (Intact > Scrambled). Slices around the significant clusters were spaced every $6mm$; all other slices were spaced every $15mm$.

starting point from which to test existing methodological techniques, and to test new methodological approaches, as illustrated later in the thesis.

The correspondence between the group statistical results for the source reconstructed MEEG and the fMRI is not good. There are several potential reasons for this. One is that MEEG and fMRI are sensitive to different types of neural activity (or that the fMRI activation occurs at times other than the N170 window localized). However, this seems unlikely given the prior intracranial EEG data cited in section 3.2, where face-specific evoked responses around $200ms$ are seen in many of the areas activated in the present fMRI analysis. Thus the poor correspondence seems more likely to reflect a problem with the MEEG inversion. One likely reason is the quality of the cortical and BEM surfaces used in SPM's forward modeling. These surfaces are not extracted directly from each participant's MRI, but indirectly by taking a set of surfaces from a canonical brain in MNI space,

and warping these to approximately match the shape of each participant's brain (based on inverting the warps used to transform their MRI to MNI space). But because no brain can be matched perfectly, there are likely to be errors in these inverse-normalized surfaces, particularly the cortical surface. **??** investigates how to better obtain such surfaces directly from each participant's MRI images, both T1 and FLASH. Another possible reason for the poor MEEG inversion results might be the type of volume conduction model. SPM uses a deformed sphere approach (Nolte, 2003) for MEG, and a 3-layer BEM for EEG ((Berg and Scherg, 1994) . In the next chapter, the MNE software package is used to construct a unified 3-layer BEM for both MEG and EEG. Yet other possible reasons for the unexpected MEEG inversion results include poor coregistration (of the digitized head-points with an imperfectly inverse-normalised canonical scalp surface) and the various stages of interpolation from the cortical surface to a volumetric image and subsequent 3D smoothing that were applied in order to use SPM's machinery for mass univariate statistics and random field theory.

Finally, another important reason for the poor MEEG inversion results is likely to be the well-known bias of the minimum norm assumption towards superficial sources (those closer to the sensors; see chapter 1 and PSFs in chapter 2). This is probably why the deeper FFA sources in the fMRI were not recovered well in the MEEG reconstruction (probably projected to more lateral and posterior regions; though this on its own would not explain the lack of left hemisphere sources in the MEEG reconstruction). This is a situation where a priori ROIs, e.g. from the fMRI might help, where knowledge of the PSFs associated with the MEEG inversion can be used to optimize estimation of electrical sources within those ROIs; an issue explored in chapter 5).

Chapter 4

Improving the Boundary Element Model through the use of Multi-Spectral MRI

4.1 Introduction

Because the quality of a Forward Model determines the quality of the resulting inverse solution, it is important to generate the Forward Model accurately. One approach to improve the Forward Model is to change the number and/or type of sensors used (as in chapter 2). Another approach is to change the Forward Model Solver (FMS), in terms of assuming a Boundary Element Model (BEM), Finite Element Model (FEM) or Finite Difference Model (FDM), and the numerical integration/approximations to Maxwell's equations that are entailed (Mosher, Leahy, and Lewis, 1999; Lew et al., 2009; Cohen and Hosaka, 1976). Here, however, a third approach is taken: improving the accuracy of the various skull and skin surfaces by better identifying the tissue boundaries from MRI images. These surfaces are important for FMSs because of the associated changes in conductivity across these surfaces (boundaries). Tissue boundary identification has received less attention to date than the previous two approaches (Ségonne et al., 2004). It is also important because the results of some of the previous work comparing different source spaces may be invalid because of the use of poorly defined BEM

surfaces, in that the amount of error in the surface geometries may exceed that contributed by the approximations of each FMS'.

BEMs assume spaces of homogeneous conductivity between surfaces. BEMs are theoretically less accurate than Finite Element methods (FEMs/FDMs), which model those spaces in terms of volume elements (voxels) that can have different conductivities (and conductivity tensors) (Tuch et al., 2001). However, BEMs are simpler and faster to calculate (indeed, none of the major freeware software packages yet offer a FMS for FEM or FDM). In this chapter, the full 102-channel magnetometer, 204-channel planar gradiometer and 70 channel EEG montage is used as suggested by the simulations in chapter 2. The calculations will focus on the BEM FMS offered by MNE, which uses linear colocation approximations (Hämäläinen and Sarvas, 1989) (coupled with removal of vertices too close to other surfaces, where these approximations break down).

In most typical realistic "head models" used for MEG/EEG today (i.e. other than various spherical approximations, which are generally less accurate (Hämäläinen and Sarvas, 1989)), at least four surfaces are defined. The first is the cortical surface, which comprises the source space (see chapter 2), and is defined by the boundary between white and grey matter (Dale and Sereno, 1993). Accurate definition of the source space has been the focus of a lot of research (Fischl, Liu, and Dale, 2001; Fischl et al., 2004a; Dale, Fischl, and Sereno, 1999; Fischl, Sereno, and Dale, 1999), due to its value in other areas of neuroscience research (Rosas et al., 2002; Kuperberg et al., 2003; Sailer et al., 2003), resulting in excellent tools for its differentiation. The next three surfaces, the critical surfaces considered in this chapter, are chosen because they divide tissue types with markedly different electrical conductivities. These are: 1) the inner skull, defined by the boundary between CSF and bone, 2) the outer skull, defined by the boundary between bone and scalp, and 3) the skin, defined by the boundary between skin and air. To aid the reader, CSF, Bone, and SCALP (which stands for Skin, Connective tissue, Aponeurosis, Loose areolar connective tissue, and the Pericranium) will be used for describing tissue types, while inner skull, outer skull, and outer skin will be used to describe surfaces, i.e. anytime inner/outer is used it refers to a surface. The geometry of these surfaces is usually represented by triangular tessellation, i.e. a mesh defined by 1) a number of vertices in 3D space, and 2) how those

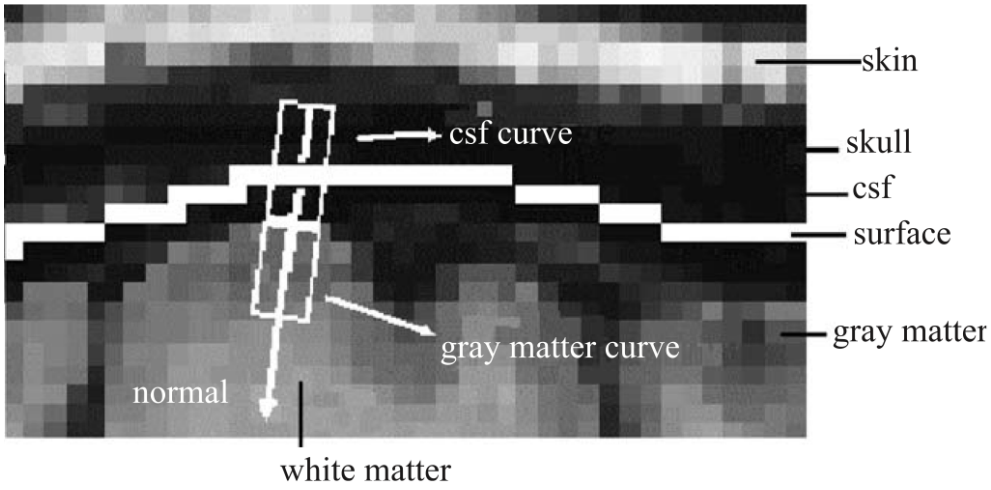

Figure 4.1: This figure (originally #17 by (Ségonne et al., 2004)) shows how the contrast in a T1-weighted MPRAGE does not differentiate between skull and CSF tissue, making the inner skull boundary (shown by white line) difficult to define, which is important for MEG/EEG forward models because this surface divides tissues with markedly different electrical conductivity.

vertices are connected to form triangular faces.

Because of the greater sensitivity of electrical than magnetic fields to the precise geometry and conductivity of the head, we know a priori that EEG results will be more sensitive to the above Forward Modeling choices. By extension, these choices affect the combination of EEG and MEG (Cuffin and Cohen, 1979; Hämäläinen et al., 1993), as used here (given the improvement in inverse solutions from combining both modalities illustrated in chapter 2). We start by considering the properties of various MR sequences that can be used to define these surfaces.

4.1.1 MRI sequences

Most current methods for defining BEM surfaces use a high resolution ($1 \times 1 \times 1mm$) T1-weighted MPRAGE/SPGR sequence. However, a T1-weighted MPRAGE does not provide good contrast between key BEM tissue types: particularly CSF and bone. This is highlighted in Figure 4.1, taken from Ségonne et al. (2004). Indeed, it is this property of MPRAGE/SPGR volumes (i.e, low intensity for CSF relative to grey/white matter, by virtue of its much longer T1 relaxation time) that makes these sequences so useful for neuroanatomical reasons

(i.e. differentiating GM and WM). Moreover, as well as resulting in negligible contrast between CSF and skull, the T1-relaxation time can vary across the skull, being shorter for Cancellous Bone / Bone Marrow, with a very low spin density across the entire skull (at echo times $> 0.5ms$ e.g. in MPRAGE/SPGR) (Haase et al., 1986; Robson et al., 2003). This produces noisy patches of medium intensity in these parts of the skull, making it even more difficult to define a clear boundary. The noisy nature is derived from the low spin density, while the short T1-relaxation time increases the intensity.

Fortunately, better contrast between these critical tissue types can be obtained from a different MR sequence: a Fast Low Angle SHot (FLASH) sequence. The value of this sequence for MEG/EEG Forward Modeling however has not been evaluated in the literature. The only previous work (unpublished) has been by Anders Dale, who used two multi-echo FLASH sequences (one at 30° flip angle and one at 5° flip angle). Data from the multiple echo times (TEs) (in this case 7) at each flip angle can be used to calculate various tissue MR parameters (T1, PD, T2*) (Deoni, Rutt, and Peters, 2003; Fischl et al., 2004b). In brief, the T1 value of a voxel can be obtained by look-up tables for combinations of flip angles or TEs or both. Once the T1 is calculated, the Proton Density (PD) is just the norm of image intensities at that voxel divided by the norm of the T1 value for unit PD. Finally, the T2* is calculated utilizing a log-linear fitting procedure applied to the different TEs. From these three MR parameters, the steady-state Bloch equation can be solved in order to generate a single FLASH volume that has "optimal" contrast between the tissue types necessary for BEM generation. The "optimal" contrast is generated because the low 5° flip angle maximizes the spin density effect (which as mentioned above has maximal contrast) and minimizes the T1-relaxation effect (which as mentioned above can vary across the skull). We call this a derived FLASH volume.

However, based on the variability of the T1-relaxation time in the skull, it seems likely that the PD volume may provide more specific information for defining BEM surfaces. This can be seen in Figure 4.2, which shows the contrasts in each of three image types: T1-weighted MPRAGE, a derived 5° FLASH volume and a FLASH-derived PD volume. The derived 5° FLASH volume appears (visually) to have better contrast than the MPRAGE for the most critical tissue

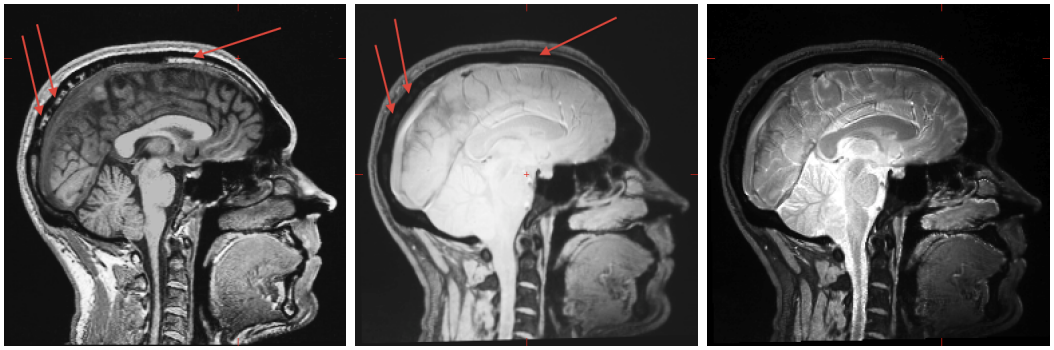

Figure 4.2: Saggital images showing the difference in tissue contrast between (from left to right): T1 weighted MPRAGE, a derived 5° FLASH volume, and a FLASH-derived PD volume. Red arrows highlight areas where T1-relaxation effects increase signal.

differentiation, i.e. between skull and other tissue-types. In particular, the red arrows in the MPRAGE image show areas in the skull with high signal (owing to T1 variation across skull tissues), which cause problems for automated surface extraction. These areas are less bright in the FLASH-derived image, but there is still residual evidence of this T1 variation. Only in the PD image has this T1-effect been sufficiently attenuated in these areas. Here I propose a new technique that utilizes this difference in the PD value to calculate the BEM surfaces, which I call the PD-derived BEM (PdBEM) method.

Finally, all three methods for extracting surfaces from an MRI volume (MPRAGE derived BEM (MdBEM), FLASH derived BEM (FdBEM), or PdBEM) were compared with a fourth approach offered with the SPM8 software (as used in chapter 3). This approach takes the pre-existing cortical, inner skull, outer skull and skin meshes from a template brain in standard (MNI) space, and warps them to approximately match the brain of each individual participant. This warping is achieved by applying the inverse of the spatial transformation needed to normalize a brain to the MNI space. This approach bypasses some of the difficulties in extracting surfaces directly from each participant's MRI images, but is generally far less accurate (given that the warps are limited to a spatial scale of approximately $10mm$ in each dimension, so cannot capture the precise cortical folding for example). We call this fourth approach the CANONICAL mesh approach

(Mattout, Henson, and Friston, 2007).

4.1.2 Evaluating Forward Models

To evaluate the quality of the BEM surfaces themselves, we can simply compare the spread of the distribution of proton densities across voxels enclosed within each of the BEM surfaces. A better method should result in a smaller spread of such values, i.e. more homogeneous tissue within that compartment. One would expect lower variance for the most homogeneous tissues. In this case, only the skull tissue definition can be expected to be homogeneous, because both the cancellous bone/marrow and cortical bone have very low proton densities. Higher variability can be expected in the "CSF" tissue, which in this case is defined as being the CSF, Grey Matter, White Matter and dural tissues, as these tissues have more variable PD. The SCALP tissue should also have more variable response, because of the variable properties of the constituent Skin, Connective tissue, Aponeuresis, Loose areolar connective tissue, Pericranium. Because the distribution of voxel intensities within each surface was not Gaussian, we used the median to quantify each distribution's central tendency and the absolute average deviation (AAD) about the median (see Equation 2.6) to quantify the spread of each distribution. Fortunately, the distributions of these metrics across participants was Gaussian, allowing standard parametric statistics to test differences across the three methods.

However, establishing the accuracy of the Forward Models resulting from each type of surface definition is difficult, because unless one uses a realistic phantom (Mosher, Leahy, and Lewis, 1999), the ground truth (with which to compare different forward models) is usually unknown. One technique is to compare the correlation between the lead-fields for each sensor that result from different choices of head model / FMS. This can quantify the extent to which the resulting forward models differ, but not which is better. A more recent technique (Henson, Mouchlianitis, and Friston, 2009) is to compare different forward models in terms of their Bayesian "model evidence" (the probability of generating the data given a model). Using a Variational Free-energy approximation to the log of the model evidence (see Friston et al. (2007) for details), one can select the forward model

(based on one of the four derivations of BEM surfaces considered here) with the highest free-energy. This approach avoids the difficulties in generating accurate life-like phantoms, though is restricted to the particular dataset under consideration (i.e. the results may not generalize to new datasets). In other words, one's inference is limited by the particular paradigm being tested. Here we used the free energy of a L2-norm inversion of the data in chapter 3 using SPM8.

4.2 Methods

The MRI parameters and MEG+EEG data preprocessing are described in chapter 3. The only deviation was that the data from one participant were not used because the FMS for the MdBEM below could not be calculated due to intersecting surfaces.

4.2.1 Surface Generation Techniques

For the main comparison of MdBEM, FdBEM and PdBEMs, the same cortical surface was used (i.e. these three forward models differed only in the BEM surfaces). The derivation of this surface in FreeSurfer is described in chapter 3. The parameters of the MPRAGE and FLASH sequences are also described in that chapter. Furthermore, for each of the techniques described below, all three of the surfaces are generated as either fourth or fifth order icosahedral surfaces (2,562 or 10,242 vertices) and downsampled to fourth order icosahedral surfaces (due to computational limitations of the FMSs employed).

4.2.1.1 MPRAGE derived BEM (MdBEM)

The surfaces were extracted from the MPRAGE image using a "hybrid" approach to skull stripping (incorporating a watershed algorithm with deformable surface models). This proceeds by identifying a white matter voxel and utilizing connected components to generate an initial estimate of the brain volume (the watershed algorithm). A smooth surface is then fitted to this volume to help correct for excluded brain matter and included non-brain matter. A pre-computed atlas of this surface is used to further adjust the geometry of the surface. Once more

smoothing is applied, this surface is grown $3mm$, forming the inner skull surface. Next, the outer skin surface is calculated by fitting a fifth order icosahedral surface to the outer edge of the MPRAGE. Based on this surface, an estimate of the outer skull surface is calculated by shrinking the outer skin surface by $3mm$. For a more detailed description of this technique, see Ségonne et al. (2004).

4.2.1.2 FLASH 5° derived BEM (FdBEM)

This technique utilizes two multi-echo FLASH sequences to generate an "optimal" FLASH sequence (Fischl et al., 2004b). The "optimal" FLASH sequence has a TR of $20ms$, a flip angle of 5°, and a TE of $5ms$. This technique begins with the skull-stripped "brain" volume generated by FreeSurfer (utilizing the hybrid watershed/template deformation skull stripping (Ségonne et al., 2004)). A fourth order icosahedron is fit around this volume and smoothed several times. The algorithm then uses this estimate to search from $3mm$ inside of the estimate, to $30mm$ outside of the estimate, for the boundary in the FLASH 5° volume. This new surface is then smoothed, making the "inner skull surface". Next the thickness of the skull is estimated from the FLASH 5° volume. The estimation begins from a $3mm$ expansion of the "inner skull surface". Stepping out from this minimum all the way to a $30mm$ maximum expansion, the algorithm searches for a preset value, indicating the boundary between the cortical bone and scalp tissues. This algorithm performs a check to make sure that the estimation does not step beyond the SCALP-air boundary. Then the "outer skin surface" is calculated by fitting a fourth order icosahedral surface around the MPRAGE volume and smoothing it.

4.2.1.3 PD derived BEM (PdBEM)

This new technique utilizes the two multi-echo FLASH sequences to generate a Proton Density (PD) volume (Deoni, Rutt, and Peters, 2003; Fischl et al., 2004b). First, a fifth order icosahedron is fit around the outside of the head to produce the outer skin surface. This surface was then used to generate a mask to remove all non-head regions from a volume. That mask was applied to the PD volume and then another icosahedron fit, this time around the low intensity voxels, creating

an initial estimate of the outer skull surface.

Finally, the PD is masked using the outer skull surface. With this masked volume, a small algorithm is run to remove any remaining eye socket and optic nerve (before it joins the cortex). This algorithm detects the anterior portion of the CSF from the masked volume, then removes any tissue which is not contiguous in the ventral direction. One final step insures that any voxels identified as GM or WM by FreeSurfer, that have been removed by the algorithm are re-incorporated into the volume. Then another icosahedron is fit to the resulting volume, generating the inner skull surface. Finally, the outer skull surface is finalized by re-estimating the low intensity voxels inside the outer skin surface. The re-estimation insures that all voxels at least $1mm$ outside the boundary of the inner skull surface are treated as low intensity.

4.2.2 SPM Meshes

One set of meshes, generated in SPM8, were also used for comparison. These meshes are generated from a set of template meshes supplied with SPM8 (`http://www.fil.ion.ucl.ac.uk/spm`). These meshes happen to be created by the author of this thesis (independent of the work reported here), using the above MdBEM algorithm on an individual from a large sample, deemed by the Montreal Neurological Institute to be most typical of that sample. The cortical mesh contained 20,484 vertices, while each of the skull/scalp meshes contained 2,652 vertices. The meshes were generated separately for each participant, by applying the inverse of SPM8's spatial transformation. SPM8 calculates a spatial transformation as part of the standard normalization and segmentation process used for fMRI analysis (Ashburner and Friston (2005) also see chapter 3). In brief, each participant's MPRAGE volume was segmented and normalized simultaneously to match template grey, white, CSF and skull/scalp probability maps in MNI space. This normalization was based on a 12-parameter affine fit, followed by nonlinear fitting of a set of $3D$ discrete cosine basis functions while simultaneously minimizing a bending energy cost function. This transformation can be approximately inverted, and then applied to the template meshes described above to warp them to approximately match each participant's individual anatomy.

4.2.3 Forward Model Solver (FMS)

The same coregistration of MRI surfaces and MEG/EEG data was used for all types of meshes, based on MNE"s Iterative Closest Point (ICP) technique (Besl and McKay, 1992). In order to maximize the accuracy of this fit, a densely ($1mm$) tessellated surface was calculated for the skin of each participant, and used for registration as described in the MNE Manual. Because the inversion was done in SPM8, the SPM8 functions were modified to allow importing of the FreeSurfer meshes and the MNE forward model (gain matrix). Due to memory limitations of the SPM code however (and for better comparison with SPM's canonical cortical mesh), the cortical meshes were limited to a maximum of 20,484 sources oriented perpendicular to the cortical surface. For the MNE/Freesurfer meshes, this was achieved by downsampling the surfaces based on the fit of their inflated surface to a fifth order icosahdral surface (`http://www.martinos.org/mne/` (Fischl, Sereno, and Dale, 1999).

For the main comparison of Md, Fd, and PdBEMs, the FMS from MNE 2.6.0 (Hämäläinen and Sarvas, 1989) was used. However the Canonical meshes from SPM8 could not easily be imported into MNE. Therefore, for these methods, the FMSs in SPM8 were used, which are actually taken from FieldTrip (`http://fieldtrip.fcdonders.nl/`). The default FieldTrip FMS offered in SPM8 uses all three surfaces for EEG (code written by Phillips C. based on (Geselowitz, 1967; Hämäläinen and Sarvas, 1989; Munck, 1992; Mosher, Leahy, and Lewis, 1999)), but only the inner skull surface for MEG (based on the Nolte method (Nolte, 2003)).

Finally, in order to provide a link between the results from the SPM8 meshes and FreeSurfer meshes (given that they differed both in the nature of the surfaces and the FMSs entailed), a final forward model was run that used FreeSurfer FdBEM and cortical meshes but SPM8/FieldTrip's FMSs.

4.2.4 Inverse Solutions

As stated above, the inversions were done using the "IID" option in SPM8, which resembles a standard L2-norm inversion, though the regularization is data-dependent, based on minimizing the model evidence within a Bayesian framework

Mattout et al., 2005. The only change from SPM8's default settings was that there was no truncation of the SVD spatial modes of the (outer-product of) the gain matrices, which meant that the dimensionality of the forward model (the total number of sensors) was matched across methods. The free energy estimate came from inverting both Faces and Scrambled faces conditions across the full epoch from $-100ms$ to $900ms$. The free energy approximation to the log model evidence for each technique was calculated. Note that SPM's scaling of the gain matrices for each sensor configuration also means that any differences in the scaling/physical units from the different FMSs should not matter.

4.3 Results

4.3.1 Surfaces

4.3.1.1 Visualisation

First we compared the three different approaches for defining the skull and scalp meshes by visual inspection of sections through various MRI images (from a randomly chosen participant's data). Figure 4.3 shows the surfaces of the MdBEM, FdBEM, and PdBEM approaches. There are two different ways to visually evaluate these techniques: via the accuracy of the boundary identification (i.e. the surfaces) and the accuracy of the tissue classification (i.e. the voxels).

Across all three views of the MdBEM we notice that the outer skin surface (as in all three techniques) performs well. However, the simple $3mm$ shrink technique employed to produce the outer skull surface yields very poor results with high intensity (i.e. not bone) voxels below this surface at all points along it. Furthermore, the inner skull surface fails to follow the CSF bone boundary in any of the three views.

The outer skin surface of the FdBEM performs very well defining the air skin boundary. However, the algorithm that estimates the outer skull based on the inner skull surface does not perform well. The most frequent errors are in locations where the skull is particularly thin: Squama temporalis and Sphenoid. The best view of these errors are highlighted (in blue arrows) in the axial slice. Furthermore, even posterior to these regions (in lime green arrows) the surface

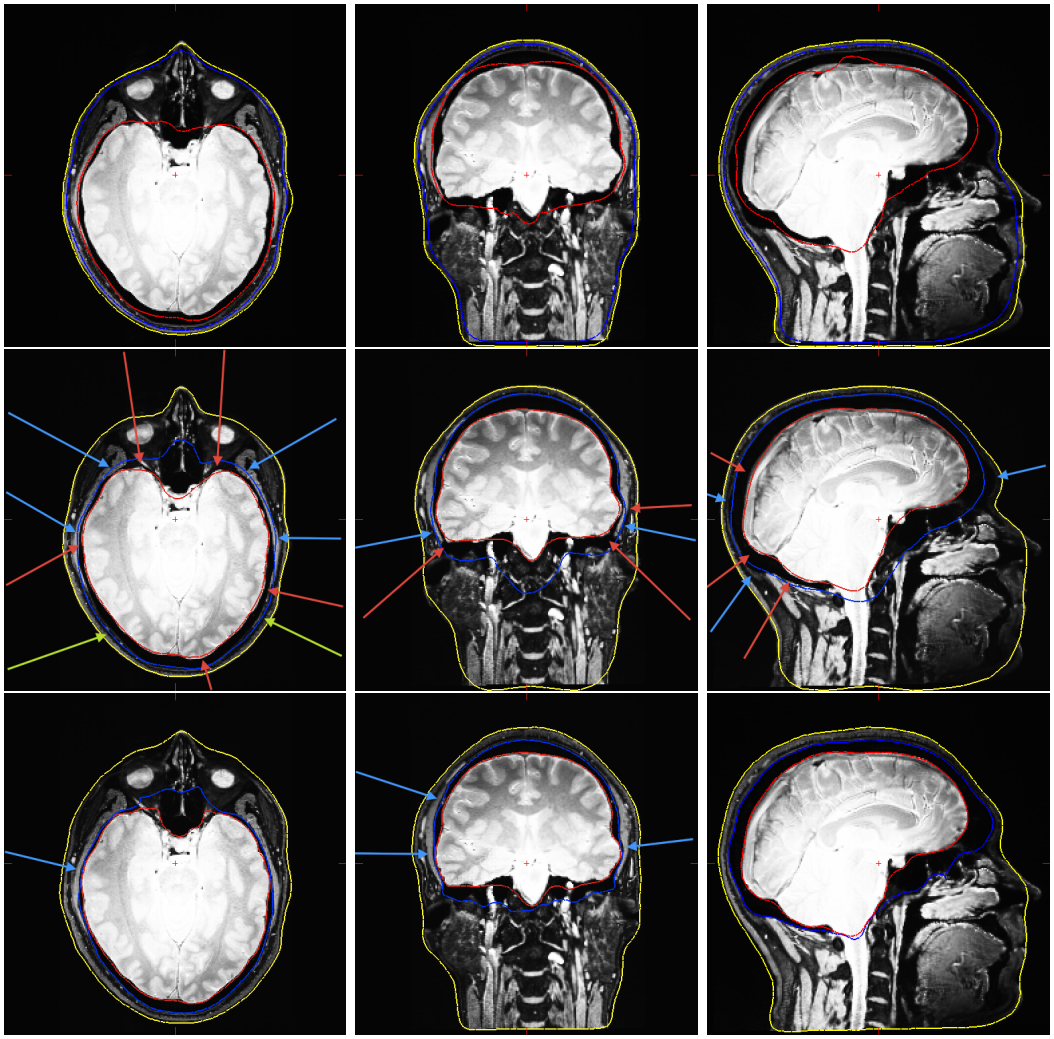

Figure 4.3: Skull/skin surfaces from the MdBEM (top row), FdBEM (middle row), and PdBEM (bottom row), displayed on PD images of a randomly selected participant. The outer skin is shown in yellow; the outer skull is shown in blue, and the inner skull is shown in red. Arrows illustrate important divergences discussed in text.

seems to miss high intensity (i.e. not bone) tissue. These regions in the Squama temporalis are also highlighted with blue arrows in the coronal slice. In the saggital slice, three regions have been highlighted (with blue arrows) where the outer skull boundary did not reach any high intensity tissue. Stepping to the inner skull surface, we find that the FdBEM often does not reach the border between high and low intensity voxels. This problem is most frequent in the occipital and temporal lobes and has been highlighted with red arrows in all three slices.

Both the outer skin and inner skull surface perform very well with the PdBEM. There are however several areas where the outer skull surface does not extend far enough out. These regions have been highlighted with blue arrows.

4.3.1.2 Quantitative Results

While we can see some differences by eye in Figure 4.3, we do not know whether these results reflect significant differences in the overall consistency/accuracy of the surfaces. One way to measure this is to estimate the spread and the center of the distribution of intensity values in the PD image across the voxels circumscribed by the three surfaces. In particular, the AAD measure of spread should be lower, the more consistent the tissue classification (i.e. the more homogeneous that classification is).

All volumes will contain some spread because of approximations/errors in the tessellation techniques and MRI partial volume effects. The main reason the PD was selected was due to its high contrast for the most critical tissue boundaries (not necessarily for consistent values of the subtissues within each classification). The boundaries between the SCALP and air, and bone, and bone and CSF all have high contrast in the PD.

However, a critical consideration in utilizing this type of analysis is how much contrast there is between the subtissues of each described tissue. Any subtissue contrast in the PD will increase the spread calculated for a "single" tissue type. As noted earlier, the SCALP compartment comprises several different tissue types: Skin, Connective tissue, Aponeurosis, Loose areolar connective tissue, and the Pericranium (and even air, for example in the nose and ear canals). As has been noted in the literature (Liang, Macfall, and Harrington, 1994), these tissues have

different MR properties i.e. T1/T2 relaxation times, resulting in different PD values. Air has the smallest PD of these (indistinguishable from noise), while muscle has a high PD (Schmitt et al., 2004). Likewise, the CSF compartment includes grey matter, white matter, and ventricular CSF (in addition to several other tissue types). Each of these tissues have different proton densities, though all of these tissues have fairly high PD values. The most relevant "misclassified" tissue for the CSF is cortical bone, which has no PD value at these TEs (Robson et al., 2003), therefore large changes in the spread of the CSF classification can still provide meaningful error quantification.

The skull tissue possesses the most extreme conductivity values relative to the other tissue types (Oostendorp, Delbeke, and Stegeman, 2000; Gonçalves et al., 2003; Lew et al., 2009). Therefore, the correct identification of this tissue is critical. There are several subtissues contained within the compartment defined by most BEM techniques: cortical bone, cancellous bone, and air (particularly in the sinuses). Fortunately, all three of these tissues have no PD values (at these TEs), so a comparison of the PD values should yield very strong evidence as to the quality of the tissue definition. The median, AAD, and total enclosed volume for each surface and each algorithm are shown in Table 4.1. In general, the AAD for

Table 4.1: The top section shows the mean across participants of the AAD measure (spread) of the voxel intensities in the PD volume; the middle section shows the mean of the medians; the bottom section contains the volume of each of the tissue classes in units of 1,000, $1mm$ isotropic voxels. A symbol is used to identify significant differences between the different algorithms (Bonferroni corrected within each column by factor of 3): $*$ different from MdBEM; † different from FdBEM; $\diamond$ different from PdBEM. See text for further details.

	Absolute Average Deviation		
Tissue	SCALP	bone	CSF
MdBEM	$17.4 \diamond \dagger$	$29.9 \diamond \dagger$	$38.9 \diamond \dagger$
FdBEM	$27.5*$	$26.4 * \diamond$	$27.0*$
PdBEM	$27.4*$	$13.4 * \dagger$	$27.5*$
	Median		
MdBEM	$47.0 \diamond \dagger$	$54.3 \diamond \dagger$	$119.5 \diamond \dagger$
FdBEM	$55.2 * \diamond$	$19.0 * \diamond$	$127.8 * \diamond$
PdBEM	$53.6 * \dagger$	$13.4 * \dagger$	$126.8 * \dagger$
	Volume		
MdBEM	$373 \diamond \dagger$	$1,802 \diamond \dagger$	$1,840 \diamond \dagger$
FdBEM	$1,864 * \diamond$	$549 * \diamond$	$1,481 * \diamond$
PdBEM	$2,137 * \dagger$	$447 * \dagger$	$1,537 * \dagger$

CSF and bone is smaller for the FdBEM and PdBEM methods than the MdBEM method (while that for the CSF is greater), but there is less difference between the FdBEM and PdBEMs. This confirms the visual results from Figure 4.3, that defining these surfaces from a T1-weighted MPRAGE sequence is generally inferior than from derived FLASH and derived PD volumes. The most important result however is that the AAD for Skull is significantly smaller for the PdBEM than FdBEM. This suggests that the new technique of defining the skull surfaces (which is most critical for the FMSs) from a PD rather than optimized FLASH image results in a more homogeneous skull volume, which is therefore likely to be more accurate.

It is noteworthy that the median PD intensity for Skull is also smaller for the PdBEM than FdBEM as predicted by the spin density results from (Haase et al., 1986; Robson et al., 2003). It is also noteworthy that, while the AAD for CSF did not differ between the FdBEM and PdBEM, there was slightly, though significantly, smaller AAD for SCALP in the FdBEM relative to PdBEM. The volume calculations show once again that the MdBEM performs strikingly differently from the FdBEM, with it having the smallest SCALP tissue definition and the largest bone and CSF tissue definition. Furthermore, while the FdBEM and PdBEM again show similar results, each of their tissue class sizes is significantly different from the others' (most notably with the bone component being smaller in the PdBEM).

4.3.2 Free Energy tests of FMS and BEM calculations

To estimate the accuracy of the Forward Models resulting from differently derived BEMs, we estimated the Bayesian model evidence for inverting the MEEG data from the paradigm in chapter 3. The results for the Free Energy approximation to the log-evidence for each type of Forward Model, for each sensor configuration, are shown in Figure 4.4. The most striking result of the tests in Figure 4.4 is that the MNE FMS significantly outperforms the SPM/Fieldtrip FMS for every sensor configuration. The next most striking result is the significant difference, when fitting the MEG data and using the MNE FMS, between the three BEM fitting techniques, with the FdBEM performing best, and MdBEM performing

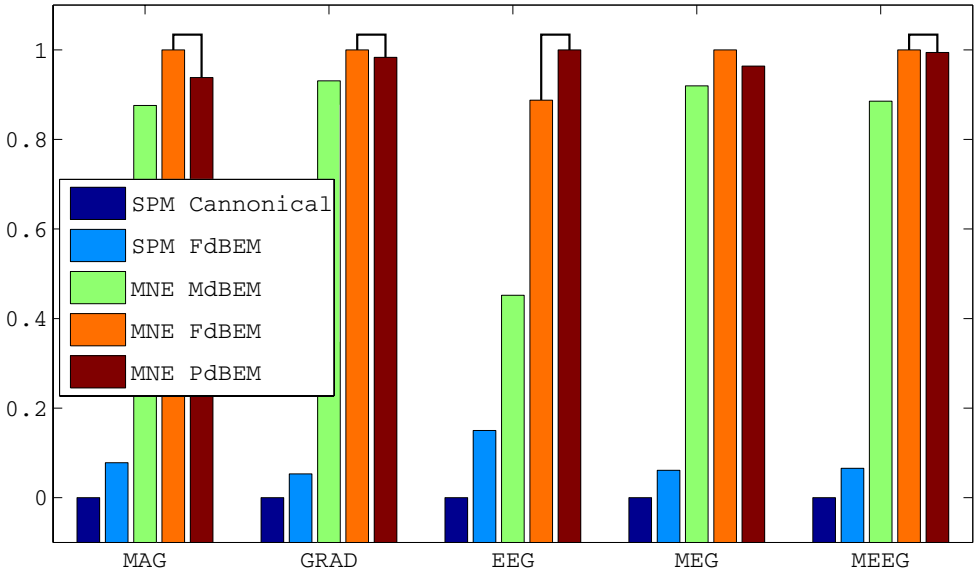

Figure 4.4: Mean across participants of the free energy approximation to model log-evidence for each type of Forward Model and each sensor configuration. Note that units of free energy are arbitrary, and cannot be compared across sensor configurations, therefore the results for each sensor configuration have been scaled by subtracting the minimum value and dividing by the maximum value (making the values range from 0 to 1). To simplify the presentation of the results, any nonsignificant difference is identified by the connection of a bar with another via a box. All other differences are significantly different following Bonferroni correction for the 10 pairwise consecutive comparisons within each sensor configuration.

worst (with PdBEM in-between). The EEG data clearly show the differences expected between the MdBEM and the F/PdBEMs (though these are replicated for each sensor configuration). The FdBEM used with the SPM/Fieldtrip FMS also outperforms SPM's Canonical meshes at every sensor configuration.

4.4 Discussion

In general, the results suggest that the FLASH and PdBEMs improve the definition the skull and scalp meshes relative to the "'standard"" MdBEM. This means that it is worthwhile taking an extra 15 minutes to acquire a FLASH sequence on each participant, whose MEG or EEG data are intended to be localized. This improvement was obvious from visual inspection, and confirmed quantitatively

via a smaller spread of PD intensities within volumes enclosed by each surface, and by a higher estimate of the Bayesian model evidence ensuing from inverting the resulting Forward Models using the data from the paradigm in chapter 3.

The present results also suggest that the author's new method of defining these surfaces directly from a PD image (PdBEM), rather than Dale"s method from an optimized FLASH image (FdBEM), can improve the definition of both the inner and outer skull surfaces (which are most critical, given the large change in electrical conductivity across these surfaces). This was suggested by visual inspection and smaller spread of PD intensities. However, the differences between these two methods did not replicate in the Log-evidence (which was actually even lower for the MEG-only sensor configuration). For this reason, coupled with the more established code for the FdBEM, the FdBEM was used for the remaining parts of this thesis. A more fine grained analysis of the data revealed that in two participants the PdBEM outperformed the FdBEM for most sensor configurations. Interestingly these two participants had the two largest CSF and bone tissue definitions by volume. This suggests that only for participants with greater space between tissue types does the PdBEM outperform the FdBEM. Therefore it is likely that these results will improve for the PdBEM when using an FMS with less error for small inter-surface distances (Gramfort et al., 2010).

Another interesting result from the free-energy approximations to the model evidence is the superior performance of the MNE FMS over the SPM/Fieldtrip FMS when inverting MEG data (and also for EEG data, though to a lesser extent). There could be a number of reasons for this, which are beyond the scope of this thesis, but it is most likely to reflect approximations in the Nolte method. The Nolte method utilizes a quasi-static approximation based on incorporating spherical harmonics to modify a spherical gain matrix. Thus it is difficult to comment on any specific differences between the Nolte approach and the Linear Collocation approach since they diverge from one another at the very start of their calculation. A final interesting result from the model evidence estimates is that BEMs derived from individual MRIs (here, FdBEMs) significantly outperform the canonical meshes used by SPM8 (even when using the same default SPM FMS, i.e. based on the Nolte method for MEG).

Nonetheless, several limitations of the above work must be remembered. Firstly,

as noted earlier, the conclusions from the model evidence estimation are conditional on the data fitted, so may not generalize to other datasets. Secondly, they are based on a limited number of vertices (due to memory limitations in SPM), such that a higher spatial resolution of the source space might change the FMS results, and introduce further differences between methods. Thirdly, the results are specific to BEMs, and the methods for extracting surfaces might show greater, or lesser, differences if one used recent advances in BEM numerical methods (Gramfort et al., 2010).

Such differences are likely to be particularly noticeable when the surfaces are very close (and the standard BEM approximations break down), such as for regions of very thin skull in the temporal lobes (see Figure 4.3). Further exploration of such FMSs is clearly warranted, but what is apparent from this chapter is that one should first ensure one can obtain the most accurate surfaces possible.

Chapter 5

Crosstalk Region Of Interest Selection: CROIS

5.1 Introduction

Neuroscientists often want to extract time-resolved data from circumscribed Regions of Interest (ROIs) within the brain that they believe to be involved in their MEEG experiment. A common approach is to estimate activity at all source locations (vertices) using a distributed inverse method, and then simply average those estimates across the vertices within each ROI. However, this approach does not take into account the point-spread/cross-talk issues associated with ill-posed linear inverse methods (discussed in chapter 2). In this Chapter, we propose a modified method for extracting data from multiple ROIs, which utilizes information about the PSF associated within a specific inverse operator, in order to minimize cross-talk between each ROI: Cross-talk Region Of Interest Selection. An important assumption here is that these are the only ROIs that are truly active; but this assumption is nearly always implicit in ROI-based analyses (and in the case of CROIS is only a "soft assumption"). Somewhat counter-intuitively, the new method entails averaging data over vertices that are not necessarily within any of the ROIs; we call these new collections of vertices "cross-talk ROIs" (cROIs). We use simulations and real data to show how the data from cROIs suffer from less cross-talk than the more conventional ROI approach.

5.2 ROIs

Take the simplest case that only a single ROI is truly active, where that ROI contains multiple point sources. As generally assumed in ROI analyses, we assume that each source within the ROI is equally active (i.e. the ROI is homogeneous). The data for an ROI could be obtained simply from the sum of the data from each enclosed source. The only problem then is that the data from these sources may not have maximum sensitivity: As the simulations in section 2.3 show, the point of greatest sensitivity for a given inversion is not necessarily the same as the true point source. Fortunately, the superposition principle means we can sum the PSFs for each source, to calculate the point of maximal sensitivity on average for that ROI, and then extract the data from this point (again, under the assumption that only this ROI is active).

The problem becomes more complicated in the case of multiple ROIs however. In this case, there can be crosstalk from one ROI to another (particularly if the ROIs are close together and share a similar dominant orientation). This means that the data extracted from some vertices within one ROI will include signal that actually comes from another ROI, i.e. the timeseries data from the ROIs will tend to be correlated with each other, owing to cross-talk, even if the true timeseries are not correlated. We start by demonstrating this using the set of 5 functionally-defined ROIs (fROIs) from our Face paradigm described in chapter 3.

5.2.1 Does this happen in practice?

In order to test this theoretical problem, we will take the Face Network of five fROIs defined by group analysis of the Faces > Scrambled faces contrast of the fMRI data in subsection 3.4.2: left Fusiform Face Area (lFFA), right Fusiform Face Area (rFFA), left Occipital Face Area (lOFA), right Occipital Face Area (rOFA) and right Superior Temporal Sulcus (rSTS) (see ahead to Figure 5.1). These fROIs are a good test bed, because they involve several different brain regions known to be co-active and close to one another.

We begin by defining a "normalized ROI PSF": the point spread function associated with an ROI that encompasses multiple vertices, assuming fixed dipoles at each vertex oriented normal to the local cortical surface. Since an fROI is

defined by an experimental contrast that is often assumed to isolate a single cognitive/neural process (such as face perception here, when contrasting faces with scrambled faces), we assume that all dipoles are equally active, with same polarity relative to the surface normal (i.e. current either in-going or out-going relative to surface). This assumption is tenable, because it corresponds to the basic tenet (often unspoken) of ROI-analyses in neuroscience: i.e. that fROIs are functionally homogeneous (if this were not the case, then one would split the fROI into smaller fROIs). In this case, the fROI PSF can be defined as the simple sum of the PSFs associated with each vertex within the ROI via the superposition principle. While vertices associated with different dipole orientations within the fROI will produce some cancellation of PSF values at other vertices (which would not happen if one took, for example, the average absolute value of each PSF), this cancellation is appropriate if the fROI vertices are truly simultaneously and equivalently active.

More precisely, and using the notation from chapter 2, the normalized PSF for each of the $r = 1 \cdots R$ ROIs involved in an experiment, $\bar{F}(r)$, is simply:

$$\bar{F}(r) = \sum_{i \in I(r)} \frac{F_i}{N_r} \tag{5.1}$$

where $I(r)$ is the set of N_r vertices within the rth ROI, and F_i is the PSF for the ith vertex. Note that ROIs are often of different size (i.e. N_r varies). Nonetheless, the area is not necessarily indicative of the strength of the activity in an ROI: large areas with weak current can produce MEG signal comparable to small areas with strong current. This is why we "normalize" the total activity displaced from an ROI (via its PSF) by number of vertices encompassed by that ROI. However, if one had independent evidence for greater activity in one ROI than another, this could be applied as an ROI-specific scaling factor.

If we take each of our 5 normalized fROI PSFs and horizontally concatenate them, we get something similar to a Point-spread Cross-talk PC matrix (only this matrix has 5 columns and N rows, where N is the number of vertices in the source space). We can compress this matrix by excluding all of the vertices that are not a part of any of the 5 fROIs. Next, we can average together the values of

the vertices of each fROI in each column. This provides us with an abbreviated PC matrix which only considers each of the 5 fROIs, i.e. the columns represent the PSF for each fROI and the rows effectively represent the CTF for each fROI (the only minor difference is that the normalization does modify the relationships of different sources to one another when N_r varies). In order to gauge how much crosstalk affects each of the sources, we can divide the values of each row by the value of the diagonal in that row, resulting in an ROI PC matrix. This will mean that the off-diagonal values will show how much activity from one fROI (column) will spread to another fROI (row) as a percentage of the recovered activity from a source in the "true" fROI. The average of 18 participants' ROI PC matrices is shown for the Face Network in Table 5.1 with no noise sources (using a Tikhonov regularization of 1/9).

Region	lFFA	rFFA	lOFA	rOFA	rSTS	n (in μAm)
lFFA	100	2	34	1	1	27
rFFA	2	100	1	15	14	19
lOFA	36	1	100	1	1	26
rOFA	1	18	2	100	7	16
rSTS	1	6	0	2	100	47

Table 5.1: Values represent the percentage of crosstalk from sources at each fROI (column) to each fROI (row), normalized by the estimated activity at that fROI (the values for each row's normalization factor (n) are given in the last column in μAm.). See text for further details.

One can see that activity spread from the lFFA to the lOFA can be 36% as high as the activity in the lFFA. In other words, in a situation where only the lFFA were truly active, there would be an appreciable probability of a false positive being detected in the lOFA. In short, extracting data from an ROI following a distributed inversion of MEEG data does not mean that data truly originates from that ROI.

5.2.2 What can we do?

If we assume that a limited number of ROIs are the only regions truly active (for the contrast of interest), then we can reduce the above problem by carefully

selecting vertices associated with each ROI that have minimal "cross-talk" from the other ROIs. Note that these vertices may not fall within any of the ROIs themselves, i.e. can be spread across the cortex, particularly if the ROIs are close and have a similar orientation (i.e. have high cross-talk). We call this set of vertices for each ROI its "cross-talk ROI" (cROI). A formal definition of cROIs is given in the following section, but in general, a cROI is a set of vertices that simultaneously possess a high PSF value for the source ROI, but low CTF values for the other destination ROIs.

5.2.3 Defining Cross-talk ROIs (cROIs)

Using the normalized ROI PSF definition in Equation 5.1, we want to find those vertices that have high PSF values for that ROI, but low CTF values from each of the other $R-1$ ROIs. We can do this by defining an "ROI cross-talk" metric, $C_i(r)$, for each of the i cortical vertices:

$$C_i(r) = \frac{\sum_{k \neq r}^{R} \left|\bar{F}_i(k)\right|}{\bar{F}(r)} \tag{5.2}$$

Note that here we do take the absolute value of the PSF, because we care about any activity spread from interfering ROIs, regardless of the polarity of activity that might be present in those ROIs. We then select the m vertices with the minimal values of $C_i(r)$. These are the vertices with the minimal ratio of total PSF values across other "interfering" ROIs relative to the PSF value for the source ROI, i.e. those vertices that have low average "cross-talk" with the other ROIs at the same time as high "point spread" with the source ROI. To get a reasonable number of vertices over which to average the data (see below), we selected $m = 100$ here to form each cROI. Note that, while we call them "cross-talk" ROIs, they are calculated using the PSFs (columns) of the original PC matrix (see chapter 2). The reason only the PSF is calculated is merely for computational convenience: the only values of Cross-talk we are interested in are those of the k ROIs. If one wanted to calculate cROIs using only the Cross-talk, one could; however, one would need to calculate the entire PC matrix. Then many of those values would be ignored: none of the columns relating to non-ROI

vertices are necessary, because CROIS ignores Cross-talk with non-ROIs. Both the PSF and the CTF are important in defining a cROI; however the critical benefit/optimization is the minimizing of Cross-talk from the other k ROIs.

5.2.4 Extracting data for cROIs

Given a specific inverse operator, let the activity estimated for the jth vertex be a_j. We could just take the straight average of activity estimated at each vertex in a cROI, or we could take the average of the absolute values. However, to further optimize the relevance of the cROI data to that predicted by the source ROI, we take a weighted average, weighted by the sign of the PSF for the target ROI:

$$A(r) = \sum_{i=1}^{m} sign(\bar{F}_i(r))a_i/m \tag{5.3}$$

In other words, even when the polarity of the activity estimated at the ith cROI vertex is negative, if this matches the polarity predicted by the source ROI PSF, then the value of $A(r)$ is increased (and conversely, when the polarities differ, $A(r)$ is decreased). One benefit of this approach is that the data from a cROI must specifically match the predictions of the ROI it replaces, thus reducing the likelihood of a cROI being affected by crosstalk from a region not included in CROIS. It also effectively doubles the number of vertices (in most situations) that can be included (over a scenario where one only took vertices whose sign matched that of the original ROI).

5.3 Methods

5.3.1 Generating the ROIs

The fROIs were initially defined as the contiguous clusters of voxels that survived $p < 0.05$, FWE-corrected for the T-test contrast of Faces versus Scrambled Faces in the group analysis of the fMRI data from 19 healthy participants. Since these statistical results were in MNI space, the voxels corresponding to the fROIs were inverse-normalized back into the native MRI space of each subject. The (trilinear)

reslicing of the group T-maps into each subject's native space entailed some voxels with smaller T-values, so a further voxel threshold of 2 was imposed. The remaining voxels were then projected to the nearest vertices in each subject's cortical surface using FreeSurfer. Because of some overlap between the fROIs in some subjects, particularly for the left OFA and left FFA (which were actually contiguous in the group results), additional anatomical constraints were imposed to separate them. For the OFA and FFA fROIs, the anatomical definitions of the Lateral Occipital and Fusiform cortex were taken from the Desikan-Killiany Atlas (Desikan et al., 2006); for the STS fROI, the anatomical definition of the Superior Temporal Sulcus was taken from the 2005 Destrieux Atlas (Fischl et al., 2004a; Destrieux et al., 2010).

5.3.2 Generating the cROIs

The cROIs were generated utilizing a forward model calculated with MNE version 2.6.0 (`www.martinos.org/mne/`). The forward model used a $1mm$ vertex spacing for the cortical layer and icosohedral surfaces (composed of 5,120 triangles each) for the inner skull, outer skull and scalp layers. These layers were defined using the Dale method on the MPRAGE and FLASH volumes (see chapter 4). Cortical vertices within $5mm$ of the inner skull boundary were removed leaving $\sim$ 285,000 vertices. In order to combine the magnetometer, gradiometer and EEG sensors into a single leadfield matrix, the gains for each sensor-type were normalized so as to produce the same average variance across sensors of each type (assuming all sources equally active)(Henson, Mouchlianitis, and Friston, 2009), i.e.

$$\hat{G}_i = \frac{G_i}{\sqrt{\frac{tr(G_i G_i^T)}{P_i}}} \tag{5.4}$$

where G_i is the gain (leadfield) matrix for the P_i sensors of the ith sensor-type. Simulated data for each sensor were then created by passing unit activity at each source within each ROI (and zero activity at every other vertex) through $\hat{G} = \begin{bmatrix} \hat{G}_1 \\ \hat{G}_2 \\ \hat{G}_3 \end{bmatrix}$. White noise (independent across sensors and time) was then added to the data, drawn from a zero-mean Gaussian distribution with variance chosen

to give a SNR of 0.5, 1, 3, or 10.

A standard $L2$ Minimum Norm Estimator was then calculated using a Tikhonov regularization, i.e.:

$$M = \hat{G}(\hat{G}\hat{G}^T + \lambda I)^{-1} \tag{5.5}$$

where I is a $N \times N$ identity matrix over the N sources. The choice of the regularization parameter λ was varied (4, 1, 1/9 and 1/100) to match the SNR. Note that each regularization results in a different cROI definition, because the inverse operator changes. This in turn changes the PSF, which is used to calculate the cROI (see Equation 5.2).

To simulate timeseries, each ROI was given a boxcar temporal profile of activity (with values of either 1 or -1), with the choice of boxcar duration chosen such that, over the whole T=32 samples, the temporal profile of each ROI was orthogonal to that of every other ROI (i.e. by doubling the boxcar period from one ROI to the next). Note that time is not actually a critical factor here (in that the inverse operators and hence cROIs are independent of time); the multiple "time" samples just serve to achieve multiple realizations of the random noise, and hence estimate an average correlation between cROI/ROI estimates. In other words, the samples could be shuffled and the same results would occur; the boxcar profiles are simply helpful to visualize the effect of crosstalk on the estimates of the originally uncorrelated sources.

5.4 Results

5.4.1 CROIS: noiseless case

Figure 5.1 shows an image of both the ROIs and cROIs for a randomly selected participant. It is important to note that these will differ for each participant. Table 5.2 replicates Table 5.1, using data from the cROIs rather than ROIs (averaged across participants). The most obvious improvement is the reduction in cross-talk from "interfering" ROIs to each cROI, confirming that the CROIS and data extraction work as planned. Furthermore, the total activity recovered for each cROI also exceeds that for their corresponding ROI.

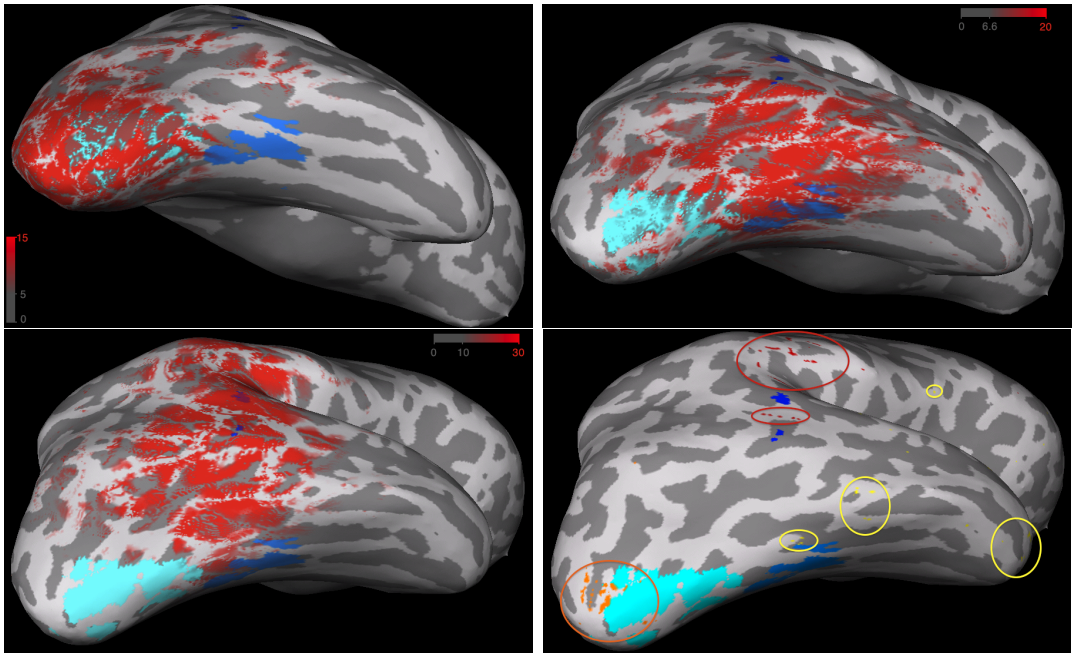

Figure 5.1: This figure shows the right hemisphere ROIs in different shades of blue (light: OFA; medium: FFA; dark: STS) on a randomly selected participant. The top left image shows the PSF (in red) of the rOFA; the top right image shows the PSF of the rFFA; the bottom left image shows the PSF of the rSTS (thresholding displayed in μAm). The participant's cROIs (with a regularization of $\lambda = 1/9$ and $m = 100$ vertices per cROI) are shown in the bottom right image (orange: OFA cROI; yellow: FFA cROI; red: STS cROI). To increase the visibility of the cROIs some of the clusters have been circled to draw the readers eye.

5.4.2 Effect of noise: CROIS timeseries

Figure 5.2 displays the estimated "timeseries" for the ROIs (left) and cROIs (right), given an SNR of 3 (probably typical of most cognitive MEEG experiments). These illustrate at a glance how cross-talk (and noise) induces correlation between ROIs, with the left plot showing greater interference between timeseries (i.e. greater deviation from the true boxcar source profiles) than the right plot. For example, the lFFA ROI (blue line in left panel), which should be uniformly positive for the first half of the epoch and uniformly negative for the second half, shows evidence of a modulation at twice this frequency, which reflects interference from the rFFA (green line). This modulation is less obvious for the lFFA cROI

	cROI Normalized					μAm	
ROI	lFFA	rFFA	lOFA	rOFA	rSTS	cROI	ROI
lFFA	100	1	0	0	0	42	27
rFFA	1	100	1	1	1	32	19
lOFA	1	1	100	1	1	56	26
rOFA	1	2	1	100	1	66	16
rSTS	0	1	0	0	100	73	47

Table 5.2: Percentage of activity "spread" from each ROI source (rows) to each cROI destination (columns), relative to the total amplitude of each cROI ($m = 100$ vertices per cROI). The final two columns show the total amplitude for each cROI and ROI (the latter repeated from Table 5.1). See text for further details.

in the right panel. (Again note that the cROI timeseries also show higher overall amplitude, as in Table 5.2.)

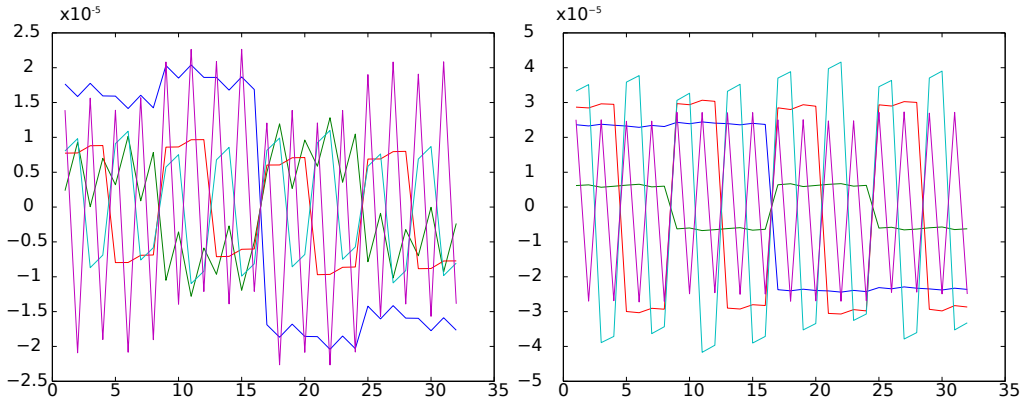

Figure 5.2: Reconstructed timeseries for ROIs (left) and cROIs (right) (blue: lFFA; green: rFFA; red: lOFA; light blue: rOFA; magenta: rSTS). The true timeseries in each ROI were orthogonal box-cars of doubling periods; see Table 5.2) for more details. Note units are μAm and the two plots have different scales.

To test this visual impression formally, we calculated the absolute value of the correlation coefficient between the estimated timeseries for each ROI/cROI and the true boxcar timeseries for each ROI/cROI (thereby discounting any differences in overall amplitude). The results for a single SNR are shown in Table 5.3. As expected, the cROIs more accurately reconstruct the temporal profile than do the

ROIs. To explore how this correlation is affected by noise levels, Figure 5.3 shows

	ROIs					cROIs				
Box	lFFA	rFFA	lOFA	rOFA	rSTS	lFFA	rFFA	lOFA	rOFA	rSTS
lFFA	0.92	0.03	0.30	0.02	0.02	1.00	0.01	0.00	0.01	0.01
rFFA	0.05	0.94	0.03	0.19	0.18	0.02	1.00	0.02	0.01	0.01
lOFA	0.34	0.02	0.89	0.04	0.01	0.01	0.01	1.00	0.02	0.01
rOFA	0.04	0.21	0.05	0.96	0.09	0.03	0.07	0.03	0.99	0.02
rSTS	0.02	0.10	0.01	0.03	0.99	0.01	0.01	0.00	0.01	1.00

Table 5.3: The mean correlation coefficient across subjects between the true and reconstructed timeseries for each ROI (left) and cROI (right) for an SNR of 3.

how the average absolute correlation for various "extraction methods" changes as a function of SNR. The red and blue lines correspond to the cROI and ROI "extraction methods" considered above. For further comparison, the magenta line corresponds to an alternative extraction method for ROIs ('100 PSF'), which is to average the timecourses from only the 100 vertices with the maximum PSF within the ROI (100 chosen to match the number used for CROIs, i.e. to match m). If there were fewer than 100 vertices within the ROI, all of the vertices were used, which only happened for the rSTS ROI in 11 of the participants. The green line corresponds to extracting the timecourse from the single vertex that has the maximal PSF value within the ROI ('Max PSF'), while the cyan line corresponds to the timecourse from the single vertex with the maximal absolute value of estimated activity within the ROI (given the specific random noise), as would happen if researchers simply select the peak of their reconstructed activity ('Peak').

The left plot shows, for each extraction method, and averaged across all 5 "target" ROIs, the average absolute correlation between the reconstructed timecourse for a target ROI and the reconstructed timecourse from each of the other four "interfering" ROIs. In other words, the values correspond to the mean of the off-diagonal terms of correlation matrices like that shown in Table 5.3 (though correlations are between reconstructed rather than true timecourses), where values closer to 0 are better. The right plot shows the absolute correlation between each target ROI and its true timecourse, averaged across all 5 ROIs (i.e. the

mean of the diagonal terms of correlation matrices like that shown in Table 5.3), where values closer to 1 are better. It is again clear that the CROIS is superior to all other extraction methods, significantly at all of the SNRs explored, both in minimizing interference (cross-talk; left plot) and more accurately recovering the true timecourse (right plot).

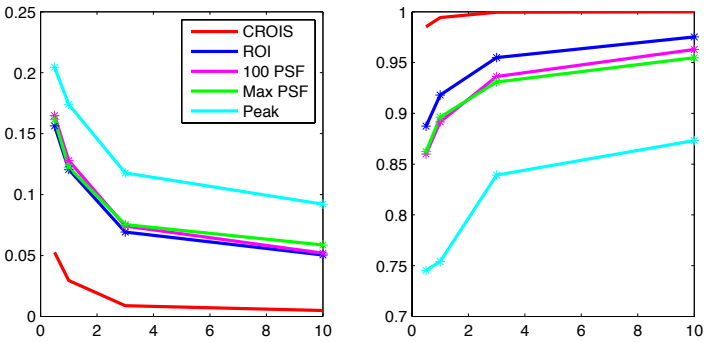

Figure 5.3: Average absolute correlation between reconstructed timeseries for "target" ROI and each "interfering" ROI (left) or between reconstructed timeseries for "target" ROI and its true timeseries (right), as a function of SNR and extraction method (indicated by color; see text for details). The significance of differences, assessed by one tailed permutation testing comparing the means, between each extraction method and CROIS is indicated by the type of symbol at each SNR point, Bonferonni-corrected for the 4 tests per SNR: $p < .05$ shown as an $*$.

5.4.3 Size of cROI

Finally, using the same simulations as above, with an SNR of 3, we explored the number of vertices used for each cROI, from m = 1:1000. As can be seen in Figure 5.4, target accuracy has an inverted "U" shape, with a peak ranging from $\approx$ 3–100 vertices, while the interference has a "U" shape with the trough ranging from $\approx$ 3–100. This can be understood in terms of the trade-off between more vertices "watering-down" the cROI effect (decreasing average target PSF and/or increasing average of interfering PSFs), but fewer vertices being more likely to be biased towards vertices that happen to have a very high target PSF (despite

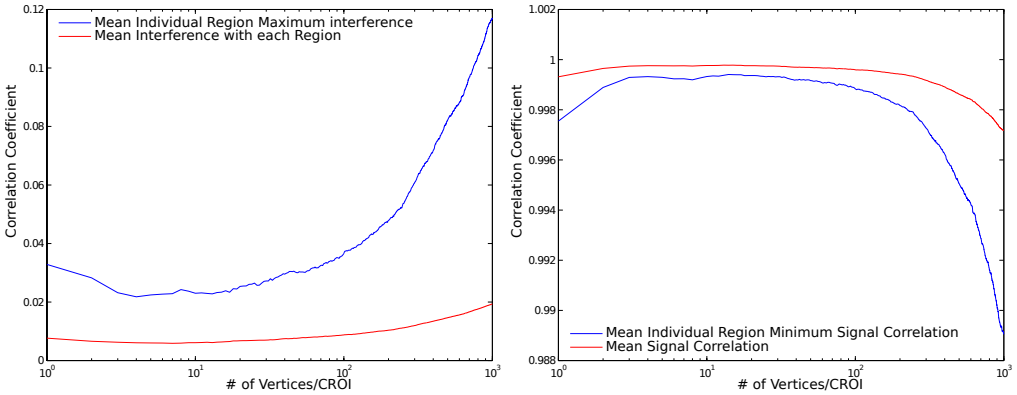

Figure 5.4: The left hand image shows how the interference changes with the number of vertices included in a cROI, while the right hand image shows how much of the signal is recovered. The blue line indicates the mean value for the cROI with the worst value, while the red line indicates the mean value across all of the cROIs.

also high interfering PSFs), or very low interference PSF from one but not all interfering ROIs.

5.4.4 True Correlations

In order to test the case when there are true correlations between ROIs, new simulated activity was generated. The simulated data in the left and right FFA are perfectly correlated (before the addition of noise). Figure 5.5 shows extracted timecourses, from which one can see by eye that the ROIs have greater variability between the lFFA and rFFA (blue and green lines) than do the cROIs. Table 5.4 shows that CROIS detect truly correlated signals better than the standard ROI approach. The mean value of the correlation between the lFFA and rFFA is significantly different ($p = 0.035$) between the CROIS (mean 0.9997) and ROI (mean 0.9624) correlation scores, as defined by one tailed permutation testing (after correction for 4 comparisons). This shows that the CROIS derived data better represented the true correlations between different regions than did ROI-derived data.

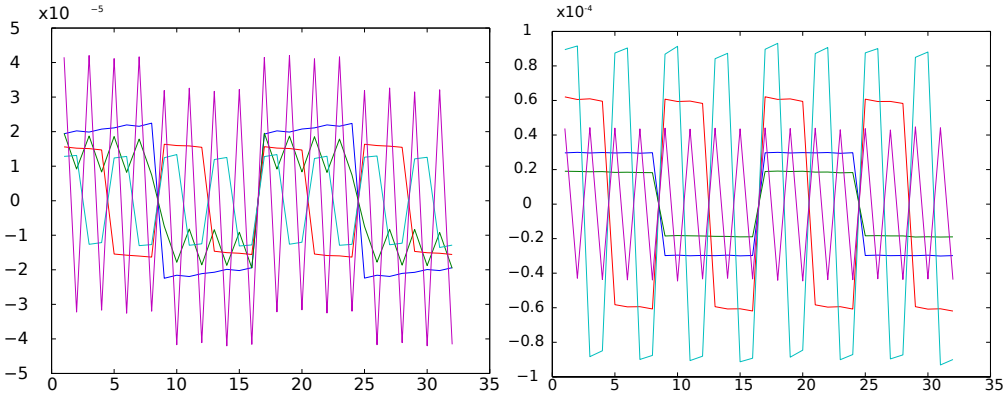

Figure 5.5: Reconstructed timeseries for ROIs (left) and cROIs (right) (blue: lFFA; green: rFFA; red: lOFA; light blue: rOFA; magenta: rSTS). The orthogonal boxcar design was used in this simulation, except that the lFFA and rFFA signals were made identical to introduce fully correlated signal. Note units are μAm and the two plots have different scales.

5.4.5 Comparison with Equivalent Current Dipoles

One may wonder how CROIS compare to an Equivalent Current Dipole (ECD) approach, where each ROI is modeled as a single dipolar source. To test this, a new five dipole leadfield was constructed. Each of the dipoles was constructed by summing the part of the leadfield used to simulate activity at each of the five ROIs. The Inverse Operator for the 5 dipole forward solution was also generated using Equation 2.1. Note that there are now only 5 columns in G, which eliminates the possibility for any third party point-spread (i.e. point-spread to a region that is not one of the sources). Table 5.5 shows the mean absolute correlation coefficient across participants. The mean of the diagonals of the dipole correlations significantly differs from the CROIS diagonals when using a one tailed permutation test Bonferroni-corrected for 4 comparisons (the correlation comparison above and three comparisons in this section). The mean difference in correlations is 0.0624, while the permutation test p-value (after correction for 4 comparisons) is 0.018. The off-diagonals (without any simulated correlation) were also significantly different: with a mean correlation difference of 0.2380($p < 0.01$ Bonferroni-corrected). The data for the ROI pairs when the nonzero lFFA-rFFA correlation was simulated revealed a mean correlation difference between techniques was 0.0881, with corrected ($p < 0.01$). These results show that CROIS

	ROIs					cROIs				
	lFFA	rFFA	lOFA	rOFA	rSTS	lFFA	rFFA	lOFA	rOFA	rSTS
lFFA	0.93	0.96	0.32	0.14	0.08	1.00	1.00	0.01	0.03	0.01
rFFA	0.93	0.96	0.32	0.14	0.08	1.00	1.00	0.01	0.03	0.01
lOFA	0.30	0.02	0.91	0.02	0.01	0.00	0.01	1.00	0.01	0.00
rOFA	0.01	0.15	0.02	0.98	0.03	0.00	0.01	0.01	1.00	0.01
rSTS	0.01	0.14	0.01	0.06	0.99	0.01	0.01	0.01	0.01	1.00

Table 5.4: The mean absolute correlation coefficient across subjects between the true and reconstructed timeseries for each ROI (left) and cROI (right) for an SNR of 3.

Table 5.5: mean absolute correlation coefficient across participants between the true and reconstructed timeseries for the ECD solution.

ROI	lFFA	rFFA	lOFA	rOFA	rSTS
lFFA	0.94	0.89	0.22	0.24	0.16
rFFA	0.94	0.89	0.22	0.24	0.16
lOFA	0.24	0.09	0.95	0.06	0.04
rOFA	0.06	0.25	0.06	0.94	0.06
rSTS	0.08	0.27	0.07	0.10	0.97

more faithfully represents uncorrelated and correlated data than both a standard ROI approach and than an ECD approach.

5.5 Real Data Test

The above simulations show that CROIS performs well with simulated white noise. However, the structure of noise in real data is unlikely to be white. Therefore, we evaluated CROIS on the face processing data described in chapter 3. With real data, we do not know the ground truth, i.e. the true source locations and their timecourses. This makes showing meaningful differences in inter-regional correlation post-stimulus impossible, because we cannot assume that the network of regions have stationary correlations. The correlation between (for example) the left OFA and left FFA is likely to vary throughout the post-stimulus period due to their various inputs. Furthermore, we cannot be confident that there will be any correlation between regions: they may have completely uncor-

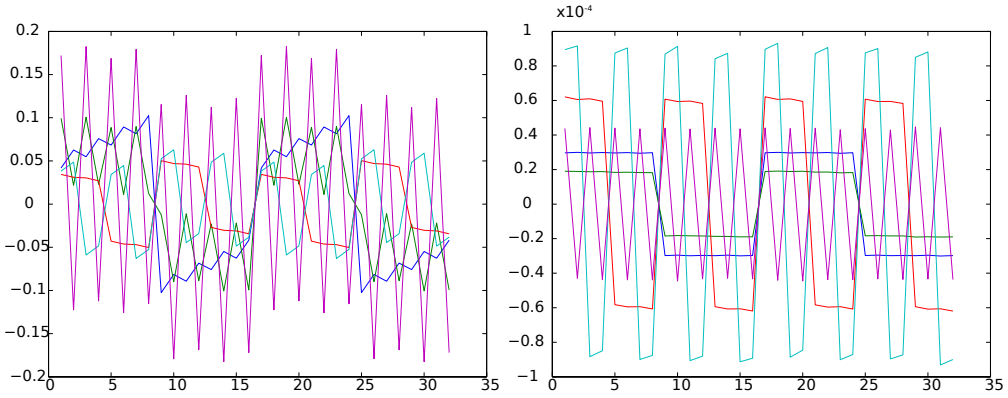

Figure 5.6: Reconstructed timeseries for dipoles (left) and cROIs (right) (blue: lFFA; green: rFFA; red: lOFA; light blue: rOFA; magenta: rSTS). The simulated data from Figure 5.5

related activity, even when they may in fact be communicating to one another (e.g. in terms of higher-order statistics, such as non-linear synchrony).

The experimental design does, however, enable us to make some assumptions about the inter-regional correlations during the pre-stimulus period. While on an individual trial basis, there is the potential for non-zero correlations in the pre-stimulus period (e.g. owing to ongoing endogenous oscillations and/or activity related to attentional/expectancy processes), when averaging the different stimuli, these potential correlations should be removed: ongoing endogenous oscillations should be eliminated by averaging, and any correlated activity related to attentional/expectancy processes should be minimized/eliminated due to the jittered pre-stimulus period ($400ms$ to $600ms$). Thus we can compare correlations between ROIs and cROIs during the 200ms pre-stimulus period, to see if cross-talk is greater in ROIs versus cROIs.

5.5.1 Inverse Operator

To calculate the inverse operator for real data, a noise covariance matrix was calculated across the $e \approx 600$ epochs (i.e. collapsing across conditions and before trial-averaging) and across the $s = 220$ samples in the pre-stimulus baseline (`http://martinos.org/mne/`). The value in this matrix for the ith and jth

sensor is then:

$$C_{ij} = \frac{1}{(es-1)} \sum_{t=1}^{es} (y_i(t) - \bar{y_i})(y_j(t) - \bar{y_j})^T \tag{5.6}$$

where $\bar{y}$ is the average over the es samples. Because this matrix can sometimes contain small eigenvalues (be deficient, particularly for EEG), it was regularized as:

$$\tilde{C} = C + \sum_{k=1}^{3} \epsilon_k \bar{\sigma}_k^2 I^{(k)} \tag{5.7}$$

where k indexes the 3 sensor-types, $\bar{\sigma}_k^2$ is the mean variance across sensors of the kth type, and I^k is the appropriate dimensionality identity matrix, and ϵ_k was set as 0.1 for all sensor-types.

The covariance matrix was scaled to match the number of averages in each condition. Having estimated the noise covariance, it was used to whiten the gain matrix and data:

$$\begin{aligned} \tilde{G} &= \tilde{C}^{-1/2} G \\ \tilde{Y} &= \tilde{C}^{-1/2} Y \end{aligned} \tag{5.8}$$

The whitened minimum-norm inverse operator can then be written as:

$$M = \tilde{R}\tilde{G}(\tilde{G}\tilde{R}\tilde{G}^T + I)^{-1} \tag{5.9}$$

where $\tilde{R} = R/\lambda^2$ is the source covariance matrix, defined such that:

$$trace(\tilde{G}\tilde{R}\tilde{G}^T) = N \tag{5.10}$$

where N is the number of sources. With this choice, λ^2 corresponds to $1/SNR$, where SNR is the (power) signal-to-noise ratio. In other words, regularization is determined by the empirical SNR, and in practice, the inverse operator can obtained simply by an SVD, as chapter 2, but this time of the whitened leadfield matrix, $\tilde{G}$.

Calculations were performed by MNE version 2.6.0 (though the whitening of the forward solution was repeated in MATLAB for the purposes of CROIS). The

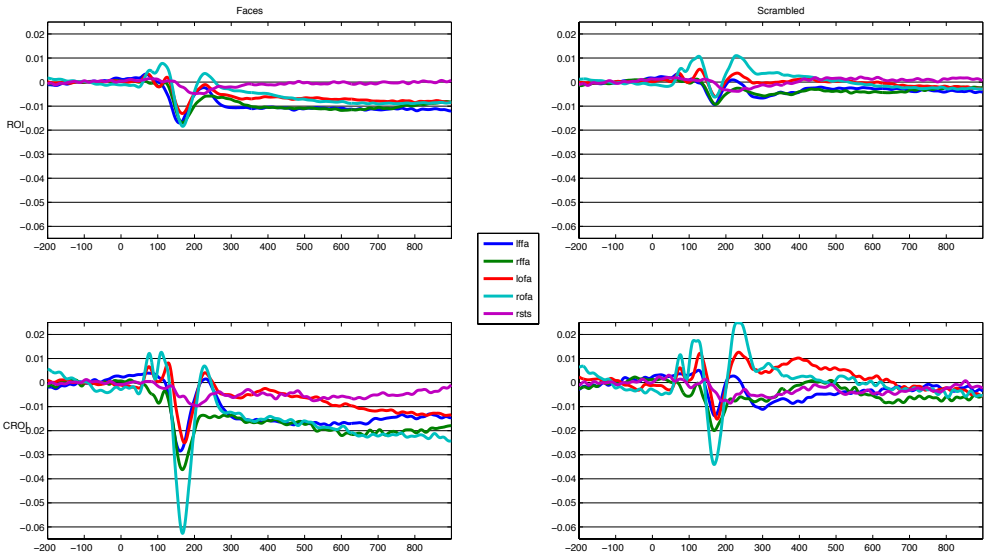

Figure 5.7: Mean evoked responses across participants for the 5 ROIs (top plots) or 5 cROIs (bottom plots), each shown in a different color, for faces (left plots) and scrambled faces (right plots).

final inverse operator was calculated in MATLAB/OCTAVE with Equation 1.2. The cROIs were recalculated utilizing the same forward matrix and inverse operator as described in Equation 5.6 to Equation 5.10.

5.5.2 Real Data Results

The mean reconstructed responses across participants from both the ROIs and cROIs are shown in Figure 5.7. Most noticeable is the "sharper" (higher amplitude) evoked responses for cROIs than ROIs. To compare these data, the Pearson correlation coefficients were computed from $-200ms$ to $0ms$ between all of the regions for ROIs and cROIs. The mean correlation of the off-diagonals for the ROIs was 0.47, while for the cROIs it was 0.33. Permutation testing revealed this difference of 0.14 to have a $p < 0.01$. This suggests that the correlation between regions is artificially inflated in the case of ROIs due to the cross-talk between regions. A corollary of this is the suggestion that CROIS can successfully reduce the cross-talk between ROIs with real data.

5.6 Discussion

We have shown that data extracted from cROIs have significantly less crosstalk than data extracted from ROIs, for both simulated and real datasets. Moreover, simulations showed that the CROIS method out-performs data taken from the top 100 PSF vertices, from the Max PSF vertex, or from the Peak vertex. This effect was significant at every SNR using simulated data from 18 participants, representing significant evidence that cROIs performed best. Visual inspection of simulated timecourses confirmed that, while sensor noise affects data extracted from both cROIs and ROIs, this effect is more pronounced for ROIs than cROIs. CROIS more faithfully represented both correlated and uncorrelated true sources. CROIS also outperformed ECDs in both cases. Finally, CROIS was able to replicate its cross-talk induced correlation reduction in data from chapter 3.

CROIS makes a number of asssumptions, most of which are shared with any ROI technique (e.g. that the ROIs are the only truly active sources and that activity within those ROIs is homogeneous). One additional assumption for CROIS however is the number of new vertices over which to extract data. The effect of this parameter m was explored, and, at least for the mesh size used here, between 3-100 vertices were optimal, reflecting a trade-off between sufficient averaging (sampling of minimal average cross-talk) and minimal dilution (from vertices with less optimal cross-talk). This also illustrates another important ingredient of CROIS analysis: a source space of $\approx 1mm$ or less distance between vertices. With this spacing, the cROIs were able to utilize approximately 100 vertices before the performance became degraded. This number of vertices provided cROIs with increased variability in the spatial distribution throughout the cortical surface. This variability reduces the risk of CROIs being susceptible to sources mistakenly excluded from the analyses, and from sources particularly susceptible to a particular noise source. The variability also improves the ability of cROIs to handle sources of error in head position estimation, because it provides several different orientation and location profiles, which increase the likelihood that some of them will be sensitive to the true activity (even though the model has errors). More simulations, beyond the scope of this study, would be necessary to examine this hypothesis.

The effect of m is further compounded by the approximately exponential relationship between source spacing and the total number of sources, i.e. approximately 2052 sources are required for a $9.9mm$ source spacing, while 20484 sources are required for a $3.1mm$ spacing (http://www.martinos.org/mne/), and $\approx$ 300,000 sources are required for the $1mm$ source spacing used in this study (though a number of these were excluded due to the inter-surface distance limitation of the BEM; see chapter 4). As a result, if one were to attempt CROIS analysis utilizing a $3.1mm$ inter-source distance spacing, based upon the m simulations and the difference in total number of vertices, one would expect only 6-–7 vertices to be utilized in a CROIS analysis. Such a small number of vertices would create a significant risk of error, in terms of random (poor) sampling of crosstalk from other ROIs. Furthermore, the above argument does not take into account the concern that, for such a decimated surface, one should be wary of using a fixed orientation constraint (given typical accuracy of such decimation). However, the Lin et al., 2006 loose orientation approach would be difficult (if at all possible) to combine with the current CROIS formulation, because CROIS depends on specific vertex activity profiles.

5.6.1 Relation to other techniques

We showed that CROIS out-performs ECD approaches. ECDs would seem, a priori, to minimize cross-talk from other vertices outside any of the ROIs. However, it does not, of course, minimize cross-talk between ROIs, as the simulations showed. Furthermore, even though this non-ROI cross-talk is excluded by the model, it is not excluded in reality, so this restricted-inversion approach would also be less robust to violations of the ROI assumption, i.e. when activity exists outside the ROIs.

One might also wonder how CROIS compares to beam-former techniques, which are designed to minimize cross-talk between ROIs. Beamformers have two major weaknesses. First, they are unable to detect extended sources well (Vrba and Robinson, 2001); second, they have difficulties detecting correlated sources (Van Veen et al., 1997; Sekihara et al., 2002). While attempts have been made at dealing with these problems (Brookes et al., 2007), they usually involve a new

assumption (e.g. pre-defining the location of correlated activity to suppress). This approach is unlikely to exist in most useful scientific cases (because both temporal and spatial information about the data are required). Second, Beamformers are less effective at dealing with neighboring regions being active, which we have shown is not a problem for CROIs (OFA and FFA bordered one another in the left hemisphere, and were extremely close in the right). Finally, beamformers depend on the data, whereas the CROIS approach here is based on a minimum norm approach that is in principle independent of the data (except when prewhitening the model based on pre-stimulus data, but other approaches to regularization can be used instead). This means that CROIs can be defined and examined in advance, without being specific to a particular dataset.

5.6.2 Conclusions

The prevalence of crosstalk means that any study utilizing ROIs should be required to display the crosstalk for each ROI. Displaying the crosstalk will enable one to determine any possible confounds in the data analysis created by the combination of the inverse solution and the analysis type. For example, if one was interpreting a face-processing study, one might erroneously attribute data from the rSTS to the rFFA, or state that processing was shared between the two, due simply to the crosstalk between those regions. Furthermore, any such ROI-based MEEG study should consider the completeness of the ROIs assumed, given that the results will change if new ROIs are added (or ROIs are dropped). Having said that, if ROIs are believed to be approximately equally active across all conditions of interest, they do not need to be included, because they cannot generate Type I error when contrasting those conditions. It is also important to note that while fMRI evidence might be sufficient for including an ROI; however, it is not sufficient for excluding an ROI, as there is not sufficient evidence to posit a linear relationship between the BOLD response and dendritic current (this also means that the relative ROI BOLD strengths should not be used to further refine a CROIS analysis).

In terms of future improvements, CROIS would benefit from using individually-defined ROIs as opposed to the group-defined ROIs used here. It would also ben-

efit from treating the BOLD data on the cortical surface differently from data in subcortical structures, to give a better estimation of the true ROI on the cortical surface (Jo et al., 2007; Jo et al., 2008; Jo et al., 2009).

Additionally, the results of the dipole analysis suggest that using fMRI results to weight a forward solution (Liu, Belliveau, and Dale, 1998) are highly dangerous and should be avoided. fMRI weighted MEEG forward solutions of the type used by Liu et al. are nearly mathematically equivalent to ECD solutions, due to the strong weighting of the source space used (Liu et al. weighted fROIs 10× all other regions). These results suggest that fMRI weighted MEEG results would likely reproduce the source activity less faithfully than both a simple ROI-approach and a CROIS approach. Furthermore, fROI weighting with non-CROIS approaches puts a strong weighting on forward solution, which reduces the detectability of non-ROI sources; however, with CROIS this is a "soft assumption", because neither the forward or inverse solutions are altered, only the data extraction therefore, when looking at the complete dataset there is no added bias from CROIS (except for the bias indicated by researchers choosing to focus on particular ROIs in the first place). In summary, CROIS offers a new approach to ROI-based MEEG analysis, which ameliorates many of the problems with the standard inverse solution.

Chapter 6

Conclusions and Discussion

The aim of this thesis was to evaluate, improve, and extend MEEG tools, and explain these in a manner accessible to most cognitive neuroscientists. Throughout the long history of MEEG (Berger, 1929; Cohen, 1968), the community has developed a rich body of knowledge and tools; however, inevitably misconceptions creep into the community (if not the literature). Several different types of MEEG tools were evaluated in this thesis: different sensor configurations; different forward models; and different data extraction techniques. In addition to dealing with these new tools, several common pitfalls in the literature were clarified and in some cases defined.

In the Introduction, the concept of Resolution was disassociated with MEEG through the use of an underdetermined example. This is the most common pitfall in the MEEG literature, because it is a common question, which the community expects has a simple answer. In much of neuroimaging, spatial resolution is a key detail in understanding the scope of a measure and motivates the question of MEEG's spatial resolution. Pairing MEEG with neuroimaging, like fMRI, yields a powerful combination, providing more detailed information about the temporal dynamics of the brain than is capable with either fMRI or MEEG alone. Just as trying to pinpoint the exact physiological temporal resolution of fMRI (for example) is virtually impossible due to the complex contributions of heart rate, respiration rate, vasculature changes, etc., trying to pinpoint the exact spatial resolution of MEEG is virtually (if not mathematically) impossible. While not having a strict resolution is the largest weakness in MEEG, it does

not negate the quality or meaningfulness of its contributions to understanding the brain's temporal dynamics (just as the lack of temporal resolution in fMRI does not negate the quality or meaningfulness of its contributions to human brain mapping). Nonetheless it is important for researchers to understand the strengths and limitations of all of the techniques in the literature in order to properly evaluate research using these tools.

Incorporating a cortical orientation constraint (Dale and Sereno, 1993) in MEEG forward modeling has been a popular recent addition to most of the major software packages. In chapter 2, some of the consequences of these modern forward solutions are explored. The first major point is that the shape of an inverse solution from one of these modern forward solutions is no longer (approximately) unimodal as in the free orientation examples used in the Introduction. One can also see that the distribution can have several peaks and troughs within even a single cm of inflated distance. This suggests that any forward model that employs a strict orientation constraint and cortical decimation is likely to introduce errors into the forward model. Researchers interested in decimating their cortical surface should incorporate techniques like loose (Lin et al., 2006) and variable loose orientation constraints when decimating their source space (or develop a different principled way to decimate the surface that addresses this issue of multimodal PSFs). Future research on this issue could provide the kick necessary to change the field's current unconcerned attitude towards mixing decimation and cortical orientation constraints.

The multimodal shape of PSFs (and CTFs) means that one cannot make the assumption that their distributions are Gaussian. Therefore, when developing techniques to compare different forward models, it is critical to use comparisons that do not rely on a specific distribution. Four such non-parametric measures were created, which avoid the often-used assumption in statistics of "normal" distributions. These measures were used to evaluate how incorporating different sensor configurations benefits source analysis when using a modern, undecimated and orientationally-constrained forward model. These measures importantly replicated the finding that combined EEG and MEG perform better than either technique alone. The measures also showed that with current forward modeling techniques, utilizing more than around 60 EEG sensors, either

combined with MEG or alone, results in little improvement in source localization. This result needs to be re-evaluated as Forward Model Solvers change, because of the possibility for improvements to the FMS to increase the ability of more sensors to discriminate differences between sources. If an FEM or FDM forward model solver became easily usable and accessible to the community, it could change these results.

In chapter 3, a dataset was presented to be used as the test-bed for the analysis throughout the subsequent chapters. The data represent an experimental design that is both simple and cognitively-relevant. The design is nearly identical in both fMRI and MEEG, contrary to many previous studies that utilize different paradigms for the two modalities, e.g. block design for fMRI and event-related for MEEG. The present dataset produces robust effects, which allow for many types of MEEG, MRI, and fMRI analyses to be examined. Multi-modal data are very useful for examining the different assumptions made both within a modality, but also across modalities, as explored throughout this thesis. This dataset has also been made freely available to the community, for whatever uses that interest them. Having a single dataset to compare different techniques is valuable to both the community and to the research presented here. The open access nature of this data offers a critical and novel type of replication only accessible in the digital age: the ability to replicate an analysis of raw data by independent researchers. Further work needs to be done expounding and encouraging this type of data sharing.

The quality of Boundary Element Models (BEMs) and Forward Model Solvers (FMSs) was explored in chapter 4. The tissue that differs most, in terms of conductivity and volume, from other tissue-types relevant to forward models is the skull. This chapter utilized an estimate of Proton Density (PD), calculated utilizing multi-spectral MRI data, to attempt a better definition of the skull tissue. The literature shows that PD (with non Ultra short Time to Echo (UTE)) should provide near zero values (depending on noise) for skull tissue. The new meshing technique based on PD data was then validated by comparing the PD values enclosed by those meshes to the PD values associated of the other meshing techniques. The PD technique yielded significantly lower PD estimates than either of the other techniques. While this technique did improve the estimates

of bone, there is significant room for further research: examining both of the different types of bone, e.g., cortical and cancellous bone, given that they exhibit different resistivities; and exploring the contributions of other tissues like Skin, Connective tissue, Adipose, Loose areolar connective tissue, and Pericranium (SCALP), which could be further subdivided.

The second component to this chapter was to compare different FMSs and meshes: the SPM/Fieldtrip FMS and the MNE FMS. In all modalities and utilizing the same meshes, the MNE FMS outperformed the SPM/Fieldtrip FMS. Interestingly, the confirmed improvement in terms of median and spread of tissue values for the PD-derived BEM meshes did not translate into the model evidence derived when comparing different inversions. While the PD-BEMs outperformed the MPRAGE-derived BEM in all modalities, it was not different from the FLASH-derived BEM in any comparison except the MEG-only comparison, where the FLASH-derived BEM outperformed it. Without further examination, we do not know what caused the discrepancy between the two analyses. The simplest explanation is that linear collocation technique with isolated skull area approach for calculating the interactions between the fields and the meshes was not sufficiently sensitive (Gramfort et al., 2010) to differentiate the layers. While other techniques are available for calculating the BEM (Gramfort et al., 2010), these techniques only became available recently and have several weaknesses in their current implementation (including a single integration point sensor model instead of the multi-point models used in MNE `http://www.martinos.org/mne/`), necessitating a complete re-write to incorporate more accurate sensor definitions. This suggests a useful future direction for this research, by either extending the symmetric BEM solutions to work with multi-point sensor integrations, or taking the next step and bringing an FDM/FEM solution to a software package designed for cognitive neuroscience.

Finally, a novel technique, CROIS, was presented for extracting data from L2 MNE solutions in chapter 5. This technique takes advantage of the intricacies of the modern forward solutions outlined in chapter 2, and the linear nature of the L2 MNE, to maximize the independence of the data extracted from source localized data. Simulations provided compelling evidence that CROIS would outperform a standard ROI approach to data extraction, when utilizing the best FMS and

meshes from chapter 4. Moreover, the baseline period of activity in the real data from chapter 3 was used to compare how CROIS versus ROI extraction would affect correlations between regions, and CROIS outperformed ROI extraction in all of these tests. While further research on CROIS is necessary to examine how different errors in MEEG analysis, e.g. errors in head position estimation, affect CROIS, the real data example suggests that the effect may not be a concern with the current accuracy levels. By incorporating the different interactions of the assumptions and techniques used in MEEG, CROIS can improve the independence of the temporal data. In addition to providing a way to avoid false correlations (caused by crosstalk), this work provides a simple way for researchers to at least evaluate the risk of these false correlations.

Throughout this thesis, each chapter has examined the relationship between the techniques being applied to analyze the data and also the physiological knowledge/assumptions of the biology. This approach is not new; it has helped scientists to correct errors in the way they approach scientific data. The surprising finding of CROIS shows that not only can this approach be used to correct errors, but it can also be used to develop new techniques, which exploit these errors. Pointspread and crosstalk are errors in the inverse solution, which can be exploited to improve the data beyond the apparent limitations of the techniques employed. Science is typically concerned with finding the truth; however, when there are hard limitations in our measurements (as we have with the Inverse Problem), we can take advantage of characterizing their imperfections in order to further improve our measurements.

In evaluating scientific techniques in neuroscience, we must not just look at one set of limitations, but evaluate all, i.e. both the physiological limitations, the physical (e.g. machine/engineering) limitations, and the analytical (software) limitations, and importantly the interactions between them. This thesis has shown that this approach is beneficial, highlighting several pitfalls and weaknesses in the current approach to MEEG analysis. It has also shown that this approach can lead to new techniques which further improve the analysis. It is important to remember that while a measurement technique may give us data in cubic voxels, no component of the human brain is cubic. Likewise while some data may be normally distributed, we need to prove that the data is normally distributed in

order to analyze it utilizing normality assumptions. Exploration of interactions of the full breadth of a dataset's limitations provides the understanding necessary to scientifically represent that data.

Bibliography

Ashburner, John and Karl J Friston (July 2005). "Unified segmentation". In: *NeuroImage* 26.3. PMID: 15955494, pp. 839–851. ISSN: 1053-8119. DOI: 10.1016/j.neuroimage.2005.02.018. URL: http://www.ncbi.nlm.nih.gov/pubmed/15955494 (visited on 06/10/2012) (cit. on pp. 43, 62).

Backus, George and Freeman Gilbert (1968). "The Resolving Power of Gross Earth Data". en. In: *Geophysical Journal of the Royal Astronomical Society* 16.2, 169–205. ISSN: 1365-246X. DOI: 10.1111/j.1365-246X.1968.tb00216.x. URL: http://onlinelibrary.wiley.com/doi/10.1111/j.1365-246X.1968.tb00216.x/abstract (visited on 06/09/2012) (cit. on pp. 5, 6).

Backus, G. and F. Gilbert (Mar. 1970). "Uniqueness in the Inversion of Inaccurate Gross Earth Data". In: *Philosophical Transactions of the Royal Society of London. Series A, Mathematical and Physical Sciences* 266.1173. ArticleType: primary_article / Full publication date: Mar. 5, 1970 / Copyright © 1970 The Royal Society, pp. 123–192. ISSN: 00804614. DOI: 10.2307/73746. URL: http://www.jstor.org/stable/73746 (visited on 02/22/2009) (cit. on p. 6).

Barry, Robert J et al. (Mar. 2003). "Preferred EEG brain states at stimulus onset in a fixed interstimulus interval auditory oddball task, and their effects on ERP components". In: *International Journal of Psychophysiology* 47.3, pp. 187–198. ISSN: 0167-8760. DOI: 10.1016/S0167-8760(02)00151-4. URL: http://www.sciencedirect.com/science/article/pii/S0167876002001514 (visited on 06/10/2012) (cit. on p. 38).

Bentin, Shlomo et al. (Jan. 2007). "Too Many Trees to See the Forest: Performance, Event-related Potential, and Functional Magnetic Resonance Imaging Manifestations of Integrative Congenital Prosopagnosia". In: *Journal of Cognitive Neuroscience* 19.1, pp. 132–146. DOI: 10.1162/jocn.2007.19.1.132. URL: http://dx.doi.org/10.1162/jocn.2007.19.1.132 (visited on 06/29/2009) (cit. on p. 35).

Berger, Hans (1929). "Über das Elektrenkephalogramm des Menschen". In: *European Archives of Psychiatry and Clinical Neuroscience* 87.1, pp. 527–570. ISSN: 0940-1334. DOI: 10.1007/BF01797193. URL: http://www.springerlink.

com/content/u1r1122ww6x285w6/abstract/ (visited on 09/15/2012) (cit. on p. 94).

Berg, P and M Scherg (Jan. 1994). "A fast method for forward computation of multiple-shell spherical head models". In: *Electroencephalography and clinical neurophysiology* 90.1. PMID: 7509274, pp. 58–64. ISSN: 0013-4694 (cit. on pp. 50, 53).

Besl, P.J. and H.D. McKay (Feb. 1992). "A method for registration of 3-D shapes". In: *IEEE Transactions on Pattern Analysis and Machine Intelligence* 14.2, pp. 239–256. ISSN: 01628828. DOI: 10.1109/34.121791. URL: http://www.computer.org/portal/web/csdl/abs/trans/tp/1992/02/i0239abs.htm (visited on 06/10/2012) (cit. on p. 63).

Brookes, Matthew J et al. (Feb. 2007). "Beamformer reconstruction of correlated sources using a modified source model". In: *NeuroImage* 34.4. PMID: 17196835, pp. 1454–1465. ISSN: 1053-8119. DOI: 10.1016/j.neuroimage.2006.11.012. URL: http://www.ncbi.nlm.nih.gov/pubmed/17196835 (visited on 06/10/2012) (cit. on p. 91).

Bruce, V and A Young (Aug. 1986). "Understanding face recognition". In: *British Journal of Psychology (London, England: 1953)* 77 (Pt 3). PMID: 3756376, pp. 305–327. ISSN: 0007-1269. URL: http://www.ncbi.nlm.nih.gov/pubmed/3756376 (visited on 06/29/2009) (cit. on p. 34).

Cohen, David (Aug. 1968). "Magnetoencephalography: Evidence of Magnetic Fields Produced by Alpha-Rhythm Currents". en. In: *Science* 161.3843, pp. 784–786. ISSN: 0036-8075, 1095-9203. DOI: 10.1126/science.161.3843.784. URL: http://www.sciencemag.org/content/161/3843/784 (visited on 09/15/2012) (cit. on p. 94).

Cohen, David and Hidehiro Hosaka (1976). "Part II magnetic field produced by a current dipole". In: *Journal of Electrocardiology* 9.4, pp. 409–417. ISSN: 0022-0736. DOI: 10.1016/S0022-0736(76)80041-6. URL: http://www.sciencedirect.com/science/article/pii/S0022073676800416 (visited on 06/09/2012) (cit. on pp. 3, 54).

Cuffin, B N and D Cohen (Aug. 1979). "Comparison of the magnetoencephalogram and electroencephalogram". In: *Electroencephalography and Clinical Neurophysiology* 47.2. PMID: 95707, pp. 132–146. ISSN: 0013-4694. URL: http://www.ncbi.nlm.nih.gov/pubmed/95707 (visited on 06/23/2009) (cit. on pp. 3, 4, 56).

Dale, A M, B Fischl, and M I Sereno (Feb. 1999). "Cortical surface-based analysis. I. Segmentation and surface reconstruction". In: *NeuroImage* 9.2. PMID: 9931268, pp. 179–194. ISSN: 1053-8119. DOI: 10.1006/nimg.1998.0395. URL: http://www.ncbi.nlm.nih.gov/pubmed/9931268 (visited on 01/30/2011) (cit. on pp. 12, 42, 55).

Dale, Anders M. and Martin I. Sereno (1993). "Improved Localization of Cortical Activity by Combining EEG and MEG with MRI Cortical Surface Reconstruction: A Linear Approach". In: *Journal of Cognitive Neuroscience* 5.2, pp. 162–176. ISSN: 0898-929X. DOI: 10.1162/jocn.1993.5.2.162. URL: http://dx.doi.org/10.1162/jocn.1993.5.2.162 (cit. on pp. 10, 55, 95).

Deoni, Sean C L, Brian K Rutt, and Terry M Peters (Mar. 2003). "Rapid combined T1 and T2 mapping using gradient recalled acquisition in the steady state". In: *Magnetic resonance in medicine: official journal of the Society of Magnetic Resonance in Medicine / Society of Magnetic Resonance in Medicine* 49.3. PMID: 12594755, pp. 515–526. ISSN: 0740-3194. DOI: 10.1002/mrm.10407. URL: http://www.ncbi.nlm.nih.gov/pubmed/12594755 (visited on 06/10/2012) (cit. on pp. 57, 61).

Desikan, Rahul S et al. (July 2006). "An automated labeling system for subdividing the human cerebral cortex on MRI scans into gyral based regions of interest". In: *NeuroImage* 31.3. PMID: 16530430, pp. 968–980. ISSN: 1053-8119. DOI: 10.1016/j.neuroimage.2006.01.021. URL: http://www.ncbi.nlm.nih.gov/pubmed/16530430 (visited on 03/22/2011) (cit. on p. 78).

Destrieux, Christophe et al. (Oct. 2010). "Automatic parcellation of human cortical gyri and sulci using standard anatomical nomenclature". In: *NeuroImage* 53.1. PMID: 20547229, pp. 1–15. ISSN: 1095-9572. DOI: 10.1016/j.neuroimage.2010.06.010. URL: http://www.ncbi.nlm.nih.gov/pubmed/20547229 (visited on 06/10/2012) (cit. on p. 78).

Eger, E. et al. (July 2005). "Familiarity enhances invariance of face representations in human ventral visual cortex: fMRI evidence". In: *NeuroImage* 26.4, pp. 1128–1139. ISSN: 1053-8119. DOI: 10.1016/j.neuroimage.2005.03.010. URL: http://www.sciencedirect.com/science/article/B6WNP-4G0DF28-4/2/ffe51218b77c5e739559c969c4175a7a (visited on 06/26/2009) (cit. on p. 36).

Fischl, B, A Liu, and A M Dale (Jan. 2001). "Automated manifold surgery: constructing geometrically accurate and topologically correct models of the human cerebral cortex". In: *IEEE Transactions on Medical Imaging* 20.1. PMID: 11293693, pp. 70–80. ISSN: 0278-0062. DOI: 10.1109/42.906426. URL: http://www.ncbi.nlm.nih.gov/pubmed/11293693 (visited on 01/30/2011) (cit. on pp. 12, 42, 55).

Fischl, Bruce et al. (Jan. 2004a). "Automatically parcellating the human cerebral cortex". In: *Cerebral Cortex (New York, N.Y.: 1991)* 14.1. PMID: 14654453, pp. 11–22. ISSN: 1047-3211. URL: http://www.ncbi.nlm.nih.gov/pubmed/14654453 (visited on 03/22/2011) (cit. on pp. 55, 78).

Fischl, Bruce et al. (2004b). "Sequence-independent segmentation of magnetic resonance images". In: *NeuroImage* 23 Suppl 1. PMID: 15501102, S69–84. ISSN: 1053-8119. DOI: 10.1016/j.neuroimage.2004.07.016. URL: http:

//www.ncbi.nlm.nih.gov/pubmed/15501102 (visited on 06/10/2012) (cit. on pp. 57, 61).

Fischl, B, M I Sereno, and A M Dale (Feb. 1999). "Cortical surface-based analysis. II: Inflation, flattening, and a surface-based coordinate system". In: *NeuroImage* 9.2. PMID: 9931269, pp. 195–207. ISSN: 1053-8119. DOI: 10.1006/nimg.1998.0396. URL: http://www.ncbi.nlm.nih.gov/pubmed/9931269 (visited on 01/30/2011) (cit. on pp. 12, 42, 55, 63).

Fisher, R. A. (1920). "Accuracy of observation, A mathematical examination of the methods of determining, by the mean error and by the mean square error". In: *Monthly Notices of the Royal Astronomical Society* 80 (cit. on p. 18).

Friston, Karl et al. (Jan. 2007). "Variational free energy and the Laplace approximation". In: *NeuroImage* 34.1. PMID: 17055746, pp. 220–234. ISSN: 1053-8119. DOI: 10.1016/j.neuroimage.2006.08.035. URL: http://www.ncbi.nlm.nih.gov/pubmed/17055746 (visited on 06/10/2012) (cit. on p. 59).

Fuchs, M et al. (May 1999). "Linear and nonlinear current density reconstructions". In: *Journal of Clinical Neurophysiology: Official Publication of the American Electroencephalographic Society* 16.3. PMID: 10426408, pp. 267–95. ISSN: 0736-0258. URL: http://www.ncbi.nlm.nih.gov/pubmed/10426408 (visited on 02/26/2009) (cit. on pp. 11, 18).

Geselowitz, D B (Jan. 1967). "On bioelectric potentials in an inhomogeneous volume conductor". In: *Biophysical journal* 7.1. PMID: 19210978, pp. 1–11. ISSN: 0006-3495. DOI: 10.1016/S0006-3495(67)86571-8. URL: http://www.ncbi.nlm.nih.gov/pubmed/19210978 (visited on 06/10/2012) (cit. on p. 63).

Gonçalves, Sónia I et al. (June 2003). "In vivo measurement of the brain and skull resistivities using an EIT-based method and realistic models for the head". In: *IEEE transactions on bio-medical engineering* 50.6. PMID: 12814242, pp. 754–767. ISSN: 0018-9294. URL: http://www.ncbi.nlm.nih.gov/pubmed/12814242 (visited on 06/10/2012) (cit. on p. 67).

Gramfort, Alexandre et al. (2010). "OpenMEEG: opensource software for quasistatic bioelectromagnetics". In: *Biomedical engineering online* 9. PMID: 20819204, p. 45. ISSN: 1475-925X. DOI: 10.1186/1475-925X-9-45. URL: http://www.ncbi.nlm.nih.gov/pubmed/20819204 (visited on 06/10/2012) (cit. on pp. 70, 71, 97).

Grave de Peralta-Menendez, R and S L Gonzalez-Andino (Apr. 1998). "A critical analysis of linear inverse solutions to the neuroelectromagnetic inverse problem". In: *IEEE Transactions on Bio-Medical Engineering* 45.4. PMID: 9556961, pp. 440–8. ISSN: 0018-9294. DOI: 10.1109/10.664200. URL: http://www.ncbi.nlm.nih.gov/pubmed/9556961 (visited on 02/23/2009) (cit. on p. 5).

Grave de Peralta Menendez, Rolando Grave, Sara L. Gonzalez Andino, and Bernd Lütkenhöner (Dec. 1996). "Figures of merit to compare distributed linear inverse solutions". In: *Brain Topography* 9.2, pp. 117–124. DOI: 10.1007/BF01200711. URL: http://dx.doi.org/10.1007/BF01200711 (visited on 02/23/2009) (cit. on pp. 5, 17).

Haase, A et al. (Apr. 1986). "FLASH imaging. Rapid NMR imaging using low flip-angle pulses". In: *Journal of Magnetic Resonance (1969)* 67.2, pp. 258–266. ISSN: 0022-2364. DOI: 10.1016/0022-2364(86)90433-6. URL: http://www.sciencedirect.com/science/article/pii/0022236486904336 (visited on 06/10/2012) (cit. on pp. 57, 68).

Halgren, E et al. (Jan. 2000). "Cognitive response profile of the human fusiform face area as determined by MEG". In: *Cerebral cortex (New York, N.Y.: 1991)* 10.1. PMID: 10639397, pp. 69–81. ISSN: 1047-3211. URL: http://www.ncbi.nlm.nih.gov/pubmed/10639397 (visited on 06/09/2012) (cit. on p. 33).

Hämäläinen, Matti et al. (Apr. 1993). "Magnetoencephalography—theory, instrumentation, and applications to noninvasive studies of the working human brain". In: *Reviews of Modern Physics* 65.2, pp. 413–497. DOI: 10.1103/RevModPhys.65.413. URL: http://link.aps.org/doi/10.1103/RevModPhys.65.413 (visited on 06/09/2012) (cit. on pp. 6, 56).

Hämäläinen, M S and R J Ilmoniemi (Jan. 1994). "Interpreting magnetic fields of the brain: minimum norm estimates". In: *Medical & Biological Engineering & Computing* 32.1. PMID: 8182960, pp. 35–42. ISSN: 0140-0118. URL: http://www.ncbi.nlm.nih.gov/pubmed/8182960 (visited on 02/24/2009) (cit. on pp. 1, 2, 11, 14).

Hämäläinen, M S and J Sarvas (Feb. 1989). "Realistic conductivity geometry model of the human head for interpretation of neuromagnetic data". In: *IEEE transactions on bio-medical engineering* 36.2. PMID: 2917762, pp. 165–171. ISSN: 0018-9294. DOI: 10.1109/10.16463. URL: http://www.ncbi.nlm.nih.gov/pubmed/2917762 (visited on 06/09/2012) (cit. on pp. 3, 4, 55, 63).

Hauk, Olaf, Daniel G. Wakeman, and Richard N. Henson (Feb. 2011). "Comparison of noise-normalized minimum norm estimates for MEG analysis using multiple resolution metrics". In: *NeuroImage* 54.3, pp. 1966–1974. ISSN: 1053-8119. DOI: 10.1016/j.neuroimage.2010.09.053. URL: http://www.sciencedirect.com/science/article/pii/S105381191001253X (visited on 06/09/2012) (cit. on p. 11).

Haxby, J. V., E. A. Hoffman, and M. I. Gobbini (2000). "The distributed human neural system for face perception". In: *Trends in Cognitive Sciences* 4.6, pp. 223–232 (cit. on pp. 33, 34).

Helmholtz, H. (1853). "Ueber einige Gesetze der Vertheilung elektrischer Ströme in körperlichen Leitern mit Anwendung auf die thierisch-elektrischen Versuche". en. In: *Annalen der Physik* 165.6, 211–233. ISSN: 1521-3889. DOI:

10.1002/andp.18531650603. URL: http://onlinelibrary.wiley.com/doi/10.1002/andp.18531650603/abstract (visited on 07/11/2012) (cit. on pp. 6, 8).

Henderson, C J, S R Butler, and A Glass (Aug. 1975). "The localization of equivalent dipoles of EEG sources by the application of electrical field theory". In: *Electroencephalography and Clinical Neurophysiology* 39.2. PMID: 50209, pp. 117–30. ISSN: 0013-4694. URL: http://www.ncbi.nlm.nih.gov/pubmed/50209 (visited on 02/20/2009) (cit. on p. 18).

Henson, Richard N., Elias Mouchlianitis, and Karl J. Friston (Aug. 2009). "MEG and EEG data fusion: Simultaneous localisation of face-evoked responses". In: *NeuroImage* 47.2, pp. 581–589. ISSN: 1053-8119. DOI: 10.1016/j.neuroimage.2009.04.063. URL: http://www.sciencedirect.com/science/article/B6WNP-4W6XVY4-9/2/c15386816666771d178766446813d459 (visited on 06/29/2009) (cit. on pp. 35, 50, 59, 78).

Henson, R. N. et al. (2003). "Electrophysiological and haemodynamic correlates of face perception, recognition and priming". In: *Cerebral Cortex* 13.7, pp. 793–805 (cit. on pp. 33, 35–37, 39, 51).

Henson, R. N. et al. (2004). "ERP and fMRI effects of lag on priming for familiar and unfamiliar faces". In: *Human Brain Mapping*, pp. 624–626 (cit. on p. 38).

Henson, R. N. et al. (2005). "Time-frequency SPMS for MEG data on face perception: Power changes and phase-locking". In: (cit. on p. 35).

Hillger, Lynn A. and Olivier Koenig (Jan. 1991). "Separable Mechanisms in Face Processing: Evidence from Hemispheric Specialization". In: *Journal of Cognitive Neuroscience* 3.1, pp. 42–58. ISSN: 0898-929X. DOI: 10.1162/jocn.1991.3.1.42. URL: http://dx.doi.org/10.1162/jocn.1991.3.1.42 (visited on 02/11/2013) (cit. on p. 34).

Ishai, Alumit (Apr. 2008). "Let's face it: It's a cortical network". In: *NeuroImage* 40.2, pp. 415–419. ISSN: 1053-8119. DOI: 10.1016/j.neuroimage.2007.10.040. URL: http://www.sciencedirect.com/science/article/B6WNP-4R33588-3/2/121b174b98952c9b7dffbcdf800d3942 (visited on 06/29/2009) (cit. on p. 35).

Jo, Hang Joon et al. (Jan. 2007). "Spatial accuracy of fMRI activation influenced by volume- and surface-based spatial smoothing techniques". In: *NeuroImage* 34.2. PMID: 17110131, pp. 550–564. ISSN: 1053-8119. DOI: 10.1016/j.neuroimage.2006.09.047. URL: http://www.ncbi.nlm.nih.gov/pubmed/17110131 (visited on 09/05/2012) (cit. on p. 93).

Jo, Hang Joon et al. (Apr. 2008). "Artificial shifting of fMRI activation localized by volume- and surface-based analyses". In: *NeuroImage* 40.3. PMID: 18291680, pp. 1077–1089. ISSN: 1053-8119. DOI: 10.1016/j.neuroimage.2007.12.036. URL: http://www.ncbi.nlm.nih.gov/pubmed/18291680 (visited on 09/05/2012) (cit. on p. 93).

Jo, Hang Joon et al. (June 2009). "Surface-based functional magnetic resonance imaging analysis of partial brain echo planar imaging data at 1.5 T". In: *Magnetic resonance imaging* 27.5. PMID: 19036544, pp. 691–700. ISSN: 1873-5894. DOI: 10.1016/j.mri.2008.09.002. URL: http://www.ncbi.nlm.nih.gov/pubmed/19036544 (visited on 09/05/2012) (cit. on p. 93).

Jones, Stephanie R et al. (Oct. 2007). "Neural correlates of tactile detection: a combined magnetoencephalography and biophysically based computational modeling study". In: *The Journal of neuroscience: the official journal of the Society for Neuroscience* 27.40. PMID: 17913909, pp. 10751–10764. ISSN: 1529-2401. DOI: 10.1523/JNEUROSCI.0482-07.2007. URL: http://www.ncbi.nlm.nih.gov/pubmed/17913909 (visited on 06/09/2012) (cit. on p. 19).

Jovicich, Jorge et al. (Apr. 2006). "Reliability in multi-site structural MRI studies: effects of gradient non-linearity correction on phantom and human data". In: *NeuroImage* 30.2. PMID: 16300968, pp. 436–43. ISSN: 1053-8119. DOI: 10.1016/j.neuroimage.2005.09.046. URL: http://www.ncbi.nlm.nih.gov/pubmed/16300968 (visited on 02/26/2009) (cit. on p. 12).

Kuperberg, Gina R et al. (Sept. 2003). "Regionally localized thinning of the cerebral cortex in schizophrenia". In: *Archives of general psychiatry* 60.9. PMID: 12963669, pp. 878–888. ISSN: 0003-990X. DOI: 10.1001/archpsyc.60.9.878. URL: http://www.ncbi.nlm.nih.gov/pubmed/12963669 (visited on 06/10/2012) (cit. on p. 55).

Landis, T et al. (June 1986). "Are unilateral right posterior cerebral lesions sufficient to cause prosopagnosia? Clinical and radiological findings in six additional patients". In: *Cortex; a journal devoted to the study of the nervous system and behavior* 22.2. PMID: 3731794, pp. 243–252. ISSN: 0010-9452 (cit. on p. 34).

Lew, Seok et al. (Sept. 2009). "Improved EEG source analysis using low-resolution conductivity estimation in a four-compartment finite element head model". In: *Human brain mapping* 30.9. PMID: 19117275, pp. 2862–2878. ISSN: 1097-0193. DOI: 10.1002/hbm.20714. URL: http://www.ncbi.nlm.nih.gov/pubmed/19117275 (visited on 06/10/2012) (cit. on pp. 54, 67).

Liang, Z, J R Macfall, and D P Harrington (1994). "Parameter estimation and tissue segmentation from multispectral MR images". In: *IEEE transactions on medical imaging* 13.3. PMID: 18218519, pp. 441–449. ISSN: 0278-0062. DOI: 10.1109/42.310875. URL: http://www.ncbi.nlm.nih.gov/pubmed/18218519 (visited on 06/10/2012) (cit. on p. 66).

Lin, Fa-Hsuan et al. (May 2006). "Assessing and improving the spatial accuracy in MEG source localization by depth-weighted minimum-norm estimates". In: *NeuroImage* 31.1. PMID: 16520063, pp. 160–71. ISSN: 1053-8119. DOI: 10.1016/j.neuroimage.2005.11.054. URL: http://www.ncbi.nlm.nih.gov/pubmed/16520063 (visited on 02/26/2009) (cit. on pp. 18, 91, 95).

Liu, A K, J W Belliveau, and A M Dale (July 1998). "Spatiotemporal imaging of human brain activity using functional MRI constrained magnetoencephalography data: Monte Carlo simulations". In: *Proceedings of the National Academy of Sciences of the United States of America* 95.15. PMID: 9671784, pp. 8945–50. ISSN: 0027-8424. URL: http://www.ncbi.nlm.nih.gov/pubmed/9671784 (visited on 02/26/2009) (cit. on pp. 5, 25, 31, 93).

Liu, Arthur K, Anders M Dale, and John W Belliveau (May 2002). "Monte Carlo simulation studies of EEG and MEG localization accuracy". In: *Human Brain Mapping* 16.1. PMID: 11870926, pp. 47–62. ISSN: 1065-9471. URL: http://www.ncbi.nlm.nih.gov/pubmed/11870926 (visited on 02/26/2009) (cit. on pp. 5, 11, 17, 25, 31).

Mattout, Jérémie, Richard N Henson, and Karl J Friston (2007). "Canonical source reconstruction for MEG". In: *Computational intelligence and neuroscience*. PMID: 18350131, p. 67613. ISSN: 1687-5265. DOI: 10.1155/2007/67613. URL: http://www.ncbi.nlm.nih.gov/pubmed/18350131 (visited on 06/10/2012) (cit. on p. 59).

Mattout, J. et al. (June 2005). "Multivariate source prelocalization (MSP): Use of functionally informed basis functions for better conditioning the MEG inverse problem". In: *NeuroImage* 26.2, pp. 356–373. ISSN: 1053-8119. DOI: 10.1016/j.neuroimage.2005.01.026. URL: http://www.sciencedirect.com/science/article/pii/S1053811905000765 (visited on 03/14/2013) (cit. on p. 64).

Menke, W. (1989). *Geophysical Data Analysis: Discrete Inverse Theory*. Academic Press (cit. on pp. 5, 6).

Molins, A et al. (Sept. 2008). "Quantification of the benefit from integrating MEG and EEG data in minimum l2-norm estimation". In: *NeuroImage* 42.3. PMID: 18602485, pp. 1069–77. ISSN: 1095-9572. DOI: 10.1016/j.neuroimage.2008.05.064. URL: http://www.ncbi.nlm.nih.gov/pubmed/18602485 (visited on 02/26/2009) (cit. on p. 11).

Mosher, J C, R M Leahy, and P S Lewis (Mar. 1999). "EEG and MEG: forward solutions for inverse methods". In: *IEEE transactions on bio-medical engineering* 46.3. PMID: 10097460, pp. 245–259. ISSN: 0018-9294. URL: http://www.ncbi.nlm.nih.gov/pubmed/10097460 (visited on 06/10/2012) (cit. on pp. 54, 59, 63).

Munck, J C de (Sept. 1992). "A linear discretization of the volume conductor boundary integral equation using analytically integrated elements". In: *IEEE transactions on bio-medical engineering* 39.9. PMID: 1473829, pp. 986–990. ISSN: 0018-9294. DOI: 10.1109/10.256433. URL: http://www.ncbi.nlm.nih.gov/pubmed/1473829 (visited on 06/10/2012) (cit. on p. 63).

Nolte, Guido (Nov. 2003). "The magnetic lead field theorem in the quasi-static approximation and its use for magnetoencephalography forward calculation

in realistic volume conductors". In: *Physics in medicine and biology* 48.22. PMID: 14680264, pp. 3637–3652. ISSN: 0031-9155. URL: http://www.ncbi.nlm.nih.gov/pubmed/14680264 (visited on 06/10/2012) (cit. on pp. 49, 53, 63).

Nunez, P. and R. Srinivasan (1981). "Electric fields of the brain: the neurophysics of EEG: Oxford University Press". In: *New York, NY* (cit. on p. 2).

Oostendorp, T F, J Delbeke, and D F Stegeman (Nov. 2000). "The conductivity of the human skull: results of in vivo and in vitro measurements". In: *IEEE transactions on bio-medical engineering* 47.11. PMID: 11077742, pp. 1487–1492. ISSN: 0018-9294. DOI: 10.1109/TBME.2000.880100. URL: http://www.ncbi.nlm.nih.gov/pubmed/11077742 (visited on 06/10/2012) (cit. on p. 67).

O Scalaidhe, S. P., F. A. W. Wilson, and P. S. Goldman-Rakic (1999). "Face-selective neurons during passive viewing and working memory performance of rhesus monkeys: evidence for intrinsic specialization of neuronal coding". In: *Cerebral Cortex* 9.5, pp. 459–475 (cit. on p. 34).

Pitcher, D. et al. (2007). "TMS evidence for the involvement of the right occipital face area in early face processing". In: *Current Biology* 17.18, pp. 1568–1573 (cit. on p. 34).

Plonsey, R and D B Heppner (Dec. 1967). "Considerations of quasi-stationarity in electrophysiological systems". In: *The Bulletin of mathematical biophysics* 29.4. PMID: 5582145, pp. 657–664. ISSN: 0007-4985. URL: http://www.ncbi.nlm.nih.gov/pubmed/5582145 (visited on 07/10/2012) (cit. on p. 3).

Puce, A, T Allison, and G McCarthy (Aug. 1999). "Electrophysiological studies of human face perception. III: Effects of top-down processing on face-specific potentials". In: *Cerebral cortex (New York, N.Y.: 1991)* 9.5. PMID: 10450890, pp. 445–458. ISSN: 1047-3211. URL: http://www.ncbi.nlm.nih.gov/pubmed/10450890 (visited on 06/09/2012) (cit. on pp. 33, 36).

Puce, A et al. (1997). "Comparison of cortical activation evoked by faces measured by intracranial field potentials and functional MRI: two case studies". In: *Human brain mapping* 5.4. PMID: 20408232, pp. 298–305. ISSN: 1065-9471. DOI: 10.1002/(SICI)1097-0193(1997)5:4<298::AID-HBM16>3.0.CO;2-A. URL: http://www.ncbi.nlm.nih.gov/pubmed/20408232 (visited on 06/09/2012) (cit. on p. 33).

Robson, Matthew D et al. (Dec. 2003). "Magnetic resonance: an introduction to ultrashort TE (UTE) imaging". In: *Journal of computer assisted tomography* 27.6. PMID: 14600447, pp. 825–846. ISSN: 0363-8715. URL: http://www.ncbi.nlm.nih.gov/pubmed/14600447 (visited on 06/10/2012) (cit. on pp. 57, 67, 68).

Rosas, H D et al. (Mar. 2002). "Regional and progressive thinning of the cortical ribbon in Huntington's disease". In: *Neurology* 58.5. PMID: 11889230, pp. 695–701. ISSN: 0028-3878 (cit. on p. 55).

Rossion, Bruno (Apr. 2008). "Constraining the cortical face network by neuroimaging studies of acquired prosopagnosia". In: *NeuroImage* 40.2, pp. 423–426. ISSN: 1053-8119. DOI: 10.1016/j.neuroimage.2007.10.047. URL: http://www.sciencedirect.com/science/article/B6WNP-4R40SM9-5/2/f2c78ce63d9fe13c2730e7b84c9e6bd2 (visited on 06/29/2009) (cit. on p. 34).

Rossion, Bruno et al. (Nov. 2003). "A network of occipito-temporal face-sensitive areas besides the right middle fusiform gyrus is necessary for normal face processing". In: *Brain* 126.11, pp. 2381–2395. DOI: 10.1093/brain/awg241. URL: http://brain.oxfordjournals.org/cgi/content/abstract/126/11/2381 (visited on 03/25/2010) (cit. on p. 33).

Sailer, Michael et al. (Aug. 2003). "Focal thinning of the cerebral cortex in multiple sclerosis". In: *Brain: a journal of neurology* 126.Pt 8. PMID: 12805100, pp. 1734–1744. ISSN: 0006-8950. DOI: 10.1093/brain/awg175. URL: http://www.ncbi.nlm.nih.gov/pubmed/12805100 (visited on 06/10/2012) (cit. on p. 55).

Sarvas, J (Jan. 1987). "Basic mathematical and electromagnetic concepts of the biomagnetic inverse problem". In: *Physics in Medicine and Biology* 32.1. PMID: 3823129, pp. 11–22. ISSN: 0031-9155. URL: http://www.ncbi.nlm.nih.gov/pubmed/3823129 (visited on 02/26/2009) (cit. on pp. 1, 11).

Schmitt, Peter et al. (Apr. 2004). "Inversion recovery TrueFISP: quantification of T(1), T(2), and spin density". In: *Magnetic resonance in medicine: official journal of the Society of Magnetic Resonance in Medicine / Society of Magnetic Resonance in Medicine* 51.4. PMID: 15065237, pp. 661–667. ISSN: 0740-3194. DOI: 10.1002/mrm.20058. URL: http://www.ncbi.nlm.nih.gov/pubmed/15065237 (visited on 06/10/2012) (cit. on p. 67).

Schweinberger, S. R. et al. (2002). "Event-related brain potential evidence for a response of inferior temporal cortex to familiar face repetitions". In: *Cognitive Brain Research* 14.3, pp. 398–409 (cit. on p. 35).

Ségonne, F. et al. (July 2004). "A hybrid approach to the skull stripping problem in MRI". In: *NeuroImage* 22.3, pp. 1060–1075. ISSN: 1053-8119. DOI: 10.1016/j.neuroimage.2004.03.032. URL: http://www.sciencedirect.com/science/article/B6WNP-4CF5CNY-1/2/33cc73136f06f019b2c11023e7a95341 (visited on 12/30/2010) (cit. on pp. 54, 56, 61).

Sekihara, Kensuke et al. (Dec. 2002). "Performance of an MEG adaptive-beamformer technique in the presence of correlated neural activities: effects on signal intensity and time-course estimates". In: *IEEE transactions on bio-medical engineering* 49.12 Pt 2. PMID: 12549735, pp. 1534–1546. ISSN: 0018-9294. URL:

http://www.ncbi.nlm.nih.gov/pubmed/12549735 (visited on 06/10/2012) (cit. on p. 91).

Sharon, Dahlia et al. (July 2007). "The advantage of combining MEG and EEG: comparison to fMRI in focally stimulated visual cortex". In: *NeuroImage* 36.4. PMID: 17532230, pp. 1225–35. ISSN: 1053-8119. DOI: 10.1016/j.neuroimage.2007.03.066. URL: http://www.ncbi.nlm.nih.gov/pubmed/17532230 (visited on 02/26/2009) (cit. on p. 18).

Taulu, S and J Simola (Apr. 2006). "Spatiotemporal signal space separation method for rejecting nearby interference in MEG measurements". In: *Physics in medicine and biology* 51.7. PMID: 16552102, pp. 1759–1768. ISSN: 0031-9155. DOI: 10.1088/0031-9155/51/7/008. URL: http://www.ncbi.nlm.nih.gov/pubmed/16552102 (visited on 06/10/2012) (cit. on p. 41).

Tsao, Doris Y., Sebastian Moeller, and Winrich A. Freiwald (Dec. 2008). "Comparing face patch systems in macaques and humans". In: *Proceedings of the National Academy of Sciences* 105.49, pp. 19514–19519. DOI: 10.1073/pnas.0809662105. URL: http://www.pnas.org/content/105/49/19514.abstract (visited on 06/29/2009) (cit. on p. 34).

Tuch, D S et al. (Sept. 2001). "Conductivity tensor mapping of the human brain using diffusion tensor MRI". In: *Proceedings of the National Academy of Sciences of the United States of America* 98.20. PMID: 11573005, pp. 11697–11701. ISSN: 0027-8424. DOI: 10.1073/pnas.171473898. URL: http://www.ncbi.nlm.nih.gov/pubmed/11573005 (visited on 01/05/2011) (cit. on p. 55).

Van Veen, B D et al. (Sept. 1997). "Localization of brain electrical activity via linearly constrained minimum variance spatial filtering". In: *IEEE transactions on bio-medical engineering* 44.9. PMID: 9282479, pp. 867–880. ISSN: 0018-9294. DOI: 10.1109/10.623056. URL: http://www.ncbi.nlm.nih.gov/pubmed/9282479 (visited on 06/10/2012) (cit. on p. 91).

Vrba, J and S E Robinson (Oct. 2001). "Signal processing in magnetoencephalography". In: *Methods (San Diego, Calif.)* 25.2. PMID: 11812209, pp. 249–271. ISSN: 1046-2023. DOI: 10.1006/meth.2001.1238. URL: http://www.ncbi.nlm.nih.gov/pubmed/11812209 (visited on 09/08/2012) (cit. on p. 91).

Young, A W et al. (Oct. 1985). "Familiarity decisions for faces presented to the left and right cerebral hemispheres". In: *Brain and cognition* 4.4. PMID: 4084403, pp. 439–450. ISSN: 0278-2626 (cit. on p. 34).

Zion-Golumbic, Elana et al. (Feb. 2008). "Human face preference in Gamma-Frequency EEG activity". In: *NeuroImage* 39.4. PMID: 18083564 PMCID: PMC2268116, pp. 1980–1987. ISSN: 1053-8119. DOI: 10.1016/j.neuroimage.2007.10.025. URL: http://www.ncbi.nlm.nih.gov/pmc/articles/PMC2268116/ (visited on 02/11/2013) (cit. on p. 35).